Space Weather

RESEARCH ARTICLE
10.1029/2024SW004245

Special Collection:
Space Weather Events of 2024 May 9-15

Unveiling Ionospheric Response to the May 2024 Superstorm With Low-Earth-Orbit Satellite Observations

Irina Zakharenkova[1], Iurii Cherniak[1], John J. Braun[1], Jan-Peter Weiss[1], Qian Wu[1,2], Teresa VanHove[1], Douglas Hunt[1], and Maggie Sleziak-Sallee[1]

[1]COSMIC Program Office, University Corporation for Atmospheric Research, Boulder, CO, USA, [2]HAO, University Corporation for Atmospheric Research, Boulder, CO, USA

Abstract The space weather event on 10–11 May 2024 was a high-impact geomagnetic storm, resulting in a SYM-H index decrease to −518 nT, the lowest level registered in several decades. We investigated the response of the Earth's ionosphere during the main phase of this storm using a comprehensive data set of ionospheric observations (in situ plasma density and/or Total Electron Content (TEC)) from twenty Low-Earth-Orbit satellites such as COSMIC-2, Swarm, GRACE-FO, Spire, DMSP, and Jason-3, orbiting at altitudes between 320 and 1,330 km. We found that ionospheric response followed a classical development pattern with the largest positive effects occurred at low and middle latitudes in daytime and evening sectors, associated with significant intensification of the Equatorial Ionization Anomaly (EIA) by the super fountain effect. The greatest effects occurred in the Pacific and American longitudinal sectors, which were in daylight, between 19 and 24 UT on 10 May 2024. This time overlaps with a period of steady southward IMF Bz and favorable conditions for long-lasting penetration electric fields. The EIA crest-to-crest separation expanded to 40–60° in latitude with the largest poleward excursion of the crest to ∼27° magnetic latitude. The extreme EIA expansion with crest separation up to 60° in latitude along with a giant plasma bite-out near the magnetic equator were observed in the dusk/evening sector over South America. The ground-based TEC showed an enhancement up to ∼200 TECU, while satellites detected an increase in topside TEC up to ∼100–155 TECU, indicating key contribution of the topside ionosphere into the ground-based TEC.

Plain Language Summary The strongest geomagnetic storm in several decades hits the Earth on 10–11 May 2024. We investigated how the Earth's ionosphere reacted to it using a massive data set of ionospheric observations from 20 satellites orbiting the Earth at various altitudes between 320 and 1,330 km. We found that ionospheric response followed a classical scenario with the largest positive effects appearing at low and middle latitudes in the daytime and evening sectors. These effects were caused by significant intensification of so called the Equatorial Ionization Anomaly (EIA). The most outstanding effects occurred in the Pacific and American longitudinal sectors, which were in daylight, between 19 and 24 UT on 10 May 2024. Two crests of EIA were displaced way more poleward from their typical locations, reaching maximal latitudinal separation up to 40–60°. The extreme EIA expansion with crest separation up to 60° in latitude along with giant plasma bite-out near the magnetic equator were observed in the evening sector over South America. Observations of ionospheric plasma concentration above multiple satellites revealed that the daytime ionosphere experienced a significant uplift to much higher altitudes than usual.

Key Points:

- Ground- and satellite-based observations revealed the largest ionospheric enhancements in the Pacific and American longitudinal sectors
- In dusk sector over Brazil Equatorial Ionization Anomaly experienced extreme crests separation up to 60° in latitude and giant plasma bite-out near the equator
- The ground-based Total Electron Content (TEC) increased up to ∼200 TECU, the largest topside TEC was up to ∼100–155 TECU

Correspondence to:
I. Zakharenkova,
irinaz@ucar.edu

Citation:
Zakharenkova, I., Cherniak, I., Braun, J. J., Weiss, J.-P., Wu, Q., VanHove, T., et al. (2025). Unveiling ionospheric response to the May 2024 superstorm with low-Earth-orbit satellite observations. *Space Weather*, *23*, e2024SW004245. https://doi.org/10.1029/2024SW004245

Received 6 NOV 2024
Accepted 18 MAR 2025

Author Contributions:
Conceptualization: Irina Zakharenkova, Iurii Cherniak, Qian Wu
Data curation: Teresa VanHove, Douglas Hunt, Maggie Sleziak-Sallee
Formal analysis: Iurii Cherniak, John J. Braun, Jan-Peter Weiss, Qian Wu, Teresa VanHove, Douglas Hunt, Maggie Sleziak-Sallee
Funding acquisition: John J. Braun, Jan-Peter Weiss
Investigation: Irina Zakharenkova, Iurii Cherniak, John J. Braun, Jan-Peter Weiss, Qian Wu

1. Introduction

In May 2024, the Earth encountered an extremely intense geomagnetic storm, ranking among the most powerful in the past few decades. To date, the May 2024 space weather event is classified as the largest geomagnetic storm of the current 25th solar cycle in terms of the SYM-H index (high resolution Dst) minimum excursion, reaching −518 nT. On the night of 10–11 May 2024, the aurora borealis was visible at remarkably low latitudes worldwide (e.g., Gonzalez-Esparza et al., 2024; Hayakawa et al., 2025). The research community studying the Magnetosphere-Ionosphere-Thermosphere coupling processes has been eagerly anticipating a geomagnetic storm of this magnitude. With a larger than ever ground-based infrastructure (e.g., thousands of Global Navigation Satellite System (GNSS) stations), numerous observational satellites in orbit, advanced physics-based and space weather prediction models, and powerful supercomputers, we have never had such comprehensive capabilities to examine the Earth's Magnetosphere-Ionosphere-Thermosphere response to such a major space weather event,

Methodology: Irina Zakharenkova, Iurii Cherniak, John J. Braun, Qian Wu
Project administration: John J. Braun, Jan-Peter Weiss
Resources: John J. Braun, Jan-Peter Weiss, Teresa VanHove, Douglas Hunt, Maggie Sleziak-Sallee
Software: Teresa VanHove, Douglas Hunt, Maggie Sleziak-Sallee
Validation: Irina Zakharenkova, Iurii Cherniak, Qian Wu, Teresa VanHove, Douglas Hunt, Maggie Sleziak-Sallee
Visualization: Irina Zakharenkova
Writing – original draft: Irina Zakharenkova, Iurii Cherniak, John J. Braun, Jan-Peter Weiss, Qian Wu, Teresa VanHove, Douglas Hunt, Maggie Sleziak-Sallee

evaluate models performance and forecasting capabilities, and assess the impact of the storm on space-based communications and navigation systems.

The May 2024 storm was the first storm with the geomagnetic three-hourly Kp index reaching its highest value of 9 since the famous "Halloween" Storm in October 2003. These conditions correspond to an "extreme" G5 level of NOAA geomagnetic storm classification (https://www.swpc.noaa.gov/noaa-scales-explanation). The dramatic ionospheric responses were reported for the super geomagnetic storms in October 2003 (e.g., Abdu et al., 2007, 2008; Basu et al., 2005; Doherty et al., 2004; Foster & Rideout, 2005; Jakowski et al., 2008; Lei et al., 2014; Lin et al., 2005; Liu & Lühr, 2005; Mannucci et al., 2005; Mitchell et al., 2005; Pokhotelov et al., 2021; Tsurutani et al., 2005, 2012; Yizengaw et al., 2005) and in November 2004 (e.g., Balan et al., 2010; Cherniak et al., 2014; Erickson et al., 2010; Fejer et al., 2007; Krankowski et al., 2007; Lei et al., 2010; Mannucci et al., 2009; Retterer et al., 2010; Wang et al., 2010). For these largest storms of the 23rd solar cycle, the SYM-H index reached a peak minimal value of −412 nT in October 2003 and –394 nT in November 2004.

The next 24th solar cycle, following an exceptionally deep solar minimum, exhibited a low level of solar activity, making it the weakest cycle in the last 100 years. The largest geomagnetic storm of the 24th solar cycle was the St. Patrick's Day storm in March 2015, with a minimum SYM-H index of −234 nT only and a maximum Kp index of 8– (7.667). Numerous publications were dedicated to investigating the effects of this storm on the Earth's ionosphere and thermosphere (e.g., Astafyeva et al., 2015; Borries et al., 2016; Carter et al., 2016; Cherniak et al., 2015; Fagundes et al., 2016; Hairston et al., 2016; Kil et al., 2016; Liu et al., 2016; Prikryl et al., 2016; Zakharenkova et al., 2016; Zhang et al., 2017), as well as numerical simulations of these effects for a better understanding of physics behind (e.g., Guo et al., 2018; Huba et al., 2017; Klimenko et al., 2018, 2019; Lu et al., 2020; Ozturk et al., 2018; Verkhoglyadova et al., 2017). Thus, the SYM-H excursion in May 2024 was at least twice the magnitude of the famous St. Patrick's Day storm in 2015 and even surpassed the magnitude of the super storms in October 2003 and November 2004, sparking exceptionally large interest in the research community.

As known during strong geomagnetic storms, the Earth's ionosphere-thermosphere system undergoes drastic modifications globally, impacting dynamics, electrodynamics, and chemistry, which can last for several days following the storm onset (Buonsanto, 1999; Mendillo, 2006; Richmond & Lu, 2000). The global changes in the composition and dynamics of this system can lead to large-scale increases and decreases in electron densities and ionospheric total electron content (TEC), which called "positive ionospheric storm" and "negative ionospheric storm," respectively. The occurrence and strength of ionospheric storm effects, both positive and negative, reveal some dependencies on location/latitude, local time, and storm phase. Negative storm effects may occur at the geomagnetic equator and high/middle latitudes mainly during the main and recovery phases of storms. A most commonly accepted mechanism for generating negative storms is neutral composition changes that lead to decrease in the O/N2 density ratio due to atmospheric disturbances driven by the enhanced Joule heating (e.g., Buonsanto, 1999; Fuller-Rowell et al., 1994; Pavlov & Foster, 2001; Prölss, 1995). Positive storms effects are more prevalent at low and middle latitudes, especially in the daytime. The positive ionospheric storms are still not well understood, and there are discussed several possible formation mechanisms, which may result in a storm-time increase in TEC and electron density: (a) neutral composition changes with an increase in the atomic oxygen (Burns et al., 1995; Fuller-Rowell et al., 1996), (b) the equatorward-directed neutral winds that drive ionospheric plasma along the geomagnetic field lines upward to where the ion loss rates are smaller (Balan et al., 2010; Jones & Rishbeth, 1971; Lin et al., 2005; Namgaladze et al., 2000), (c) the storm-induced electric fields uplifting the plasma (Abdu et al., 2008; Forbes, 1989; Huang, Foster, Goncharenko, et al., 2005; Huang, Foster, & Kelley, 2005; Kelley et al., 2004; Wang et al., 2010), (d) downward plasma fluxes from the plasmasphere (Förster & Jakowski, 2000).

In the present paper, we analyze the positive storm effects during the main phase of the May 2024 geomagnetic storm using ground-based GNSS TEC and space-based LEO observations of TEC and in situ density from COSMIC-2, Swarm, GRACE-FO, Spire, DMSP, and Jason-3 satellites.

2. Database

To analyze the Earth's ionosphere response to the May 2024 geomagnetic storm, we use the following observational data set:

2.1. Ground-Based GNSS TEC Observations

We utilize measurements from 6,000+ ground-based Global Navigation Satellite Systems (GNSS) stations. For this study, we use GNSS signals provided by the GPS, GLONASS, Galielo, and BeiDou systems. For each link receiver–satellite with an elevation cutoff of 20°, we calculate values of vertical total electron content (TEC). Details on TEC processing from raw GNSS measurements can be found in Zakharenkova et al. (2016). Further, the obtained vertical TEC values are binned into a geographic grid with 1.0° latitude and longitude spacing to produce the global maps at 10-min intervals. The high-resolution TEC maps show storm-induced dynamics of ionospheric density in space and time.

2.2. Multi-Instrument COSMIC-2 (Constellation Observing System for Meteorology, Ionosphere, and Climate) Observations

To date, the COSMIC-2 is the largest equatorial multi-satellite constellation (six satellites) designed to study the equatorial ionosphere (Weiss et al., 2022). The scientific payloads of the COSMIC-2 mission includes an advanced GNSS receiver supporting multiple measurements including multi-GNSS TEC above and below satellite altitude, radio occultation electron density profiles, amplitude and phase scintillations. Each satellite carries an Ion Velocity Meter (IVM) instrument, like the one onboard the Ionospheric Connections Explorer satellite (Heelis et al., 2017), to measure in situ ion density, composition, and temperature along the low inclination satellite orbits at ∼525–550 km altitude. COSMIC-2 observations are processed and provided by the UCAR COSMIC Data Analysis and Archive Center (CDAAC). In this study, we used a "ivmLv2" Level-2 product that contains 1 Hz total ion density (Ni) observations from six COSMIC-2 satellites and the density was calibrated using the COSMIC-2 GNSS observations (Chou et al., 2021; Wu et al., 2022) to analyze development of the ionospheric storm effects. Additionally, we utilized COSMIC-2 topside absolute TEC observations provided as a "podTc2" Level-1b product. The accuracy of the COSMIC-2 absolute TEC observations is below 3 TECU for both GPS and GLONASS (Pedatella et al., 2021, 2023). Vertical TEC values were computed from the slant TEC data with elevation angles above 10°; the mean value of simultaneous vertical TEC observations was then calculated along the satellite orbit.

2.3. Swarm Satellite Observations

The European Space Agency (ESA) Swarm mission consists of the three identical satellites—A, B, and C. Two satellites (A and C) operate in a tandem at ∼475–km altitude (as of May 2024), and the third one (Swarm–B) flies ∼40 km higher. The satellites have polar orbits with ∼88° inclination. In situ electron density (Ne) data measured by the two Langmuir Probes onboard each satellite. Additionally, each satellite has a GPS receiver tracking up to eight GPS satellites at 1 Hz. The GPS observations are used to reconstruct the topside TEC (above the Swarm orbit). The Swarm in situ density data is accessible as a "EFIxLPI_1B" Level-1b product and the absolute TEC data as a "TECxTMS_2F" Level-2 product through the ESA Earth Online portal. More description on these products is given in documents (Swarm L2 TEC Product Description, 2017; Review of Swarm L1B data quality, 2020). On 10 May 2024, the descending/ascending nodes for Swarm–A/Swarm–C and Swarm–B occurred at approximately 19.1/7.1 LT and 11.0/23.0 LT, respectively.

2.4. GRACE-FO (Gravity Recovery and Climate Experiment Follow-On) Observations

The GRACE-FO, launched in 2018, is a continuation of the original GRACE mission with near the same hardware to measure the Earth's gravity field. Maintaining a ∼220 km distance, the twin satellites follow the same orbit. In May 2024, the near-polar orbit (89° inclination) had an altitude of ∼490 km. For ionospheric research, this mission offers the topside TEC (above the orbit) data from GPS measurements and in situ density data derived from signal measurements of the K-band Ranging system (KBR) between the two GRACE-FO satellites. The technique of the Ne retrieval from the GRACE KBR measurements was described in detail by Xiong et al. (2010). The GRACE-FO ionospheric products are provided by GFZ (German Research Center for Geosciences). More details on their processing and validation can be found in a recent paper by Schreiter et al. (2023). For the May 2024 storm study, we used GRACE-FO descending passes that crossed the equator around 17.1 LT.

2.5. Spire Observations

The Spire constellation consists of multiple 3U CubeSats, sometimes numbering in the dozens in orbit. Satellites are positioned in a range of LEO orbits, with altitudes between 400 and 600 km, covering both equatorial inclinations and sun synchronous orbits. More details on ionospheric observations from the Spire mission can be found in Angling et al. (2021). GPS observations from the POD antenna were processed by the UCAR CDAAC to retrieve calibrated absolute topside TEC observations as a "podTec" Level-1b product in a similar way as for the COSMIC-2 products.

2.6. DMSP (Defense Meteorological Satellite Program) Observations

We also used in situ ion density (Ni) data from the DMSP F17 and F18 satellites, orbiting at a significantly higher altitude (~850 km). The DMSP satellites are equipped with SSIES (Special Sensors for Ions, Electrons, and Scintillation) instrument package, which includes a Retarding Potential Analyzer and an Ion Drift Meter for measuring the total ion density and drifts in the topside ionosphere (Greenspan et al., 1986; Hairston & Heelis, 1996). As of 10 May 2024, the local times of the ascending nodes for the F17 and F18 satellites were ~18.3 LT and ~15.9 LT, respectively.

2.7. Jason-3 Downward-Looking TEC Observations

Jason-3 is a satellite altimeter mission flying at a circular orbit at ~1,330 km altitude with an orbit inclination of ~66°. Measurements provided by a dual-frequency nadir-looking radar altimeter Poseidon-3B operating at 13.575 GHz (Ku-band) can be used to estimate an ionospheric electron content below the Jason-3 orbit (~1,330 km) but over the ocean/sea surface only (Jason-3 Products Handbook, 2020).

2.8. Global Electron Content (GEC)

Nowadays, the ground-based GNSS TEC becomes one of the key parameters to specify the ionospheric density. Afraimovich et al. (2008) introduced a novel method for calculating the Global Electron Content (GEC), defined as the total number of electrons in the near-Earth space environment within the GPS orbital altitude of ~20,000 km. The advantage of GEC parameter is the possibility to quantify and to analyze the global characteristics in the variability of the ionosphere/plasmasphere as a whole system, while excluding regional details. To calculate GEC, we used the Global Ionospheric Maps (GIMs) of TEC produced by the International GNSS Service (IGS). Several IGS Associate Analysis Centers generate the GIMs, which have a grid resolution of $2.5° \times 5.0°$ in latitude/longitude and time resolution of 1–2 hr. Detailed description of the IGS GIMs computation and validation can be found in the paper (Hernández-Pajares et al., 2009). Here, we used the GIM product provided by UPC (Technical University of Catalonia, Barcelona, Spain), given its higher 15–min temporal resolution. The GEC has been calculated as a sum of the TEC from each cell of the IGS TEC map multiplied by the cell area. TEC is typically quantified in TEC units, where 1 TECU equivalent to 10^{16} electrons/m^2. To measure GEC, Afraimovich et al. (2008) suggested GEC units, where 1 GECU equals to 10^{32} electrons/m^2.

3. The 10–11 May 2024 Geomagnetic Storm: Interplanetary and Geomagnetic Conditions

A series of several successive Earth-directed coronal mass ejections (CMEs), released by the highly active sunspot region AR13664 (e.g., Hayakawa et al., 2025), resulted in an "extreme" geomagnetic storm (G5 in NOAA's space weather G-scale) on the Earth on 10–12 May 2024. The storm occurred during the period of increased solar activity, close to the maximum of the current 25th solar cycle. In May 2024, the monthly average value of the F10.7 flux was ~190, while its daily value peaked at 237 during the storm.

Figure 1 presents variations of the solar wind, interplanetary, and geophysical parameters during 9–12 May 2024. The Sudden Storm Commencement (SSC) was registered at 17:05 UT on 10 May 2024 with a rapid increase of solar wind velocity, going from ~450 km/s to 700 km/s (Figure 1b), and of solar wind pressure from ~6 to 49 nPa (Figure 1c). The solar wind dynamic pressure remained at a high level of 40–50 nPa for several hours until ~22 UT. The geomagnetic three-hourly Kp index immediately reached value of 8+ at 18 UT on 10 May 2024, and remained at a high level (8–9) until 15–18 UT on 11 May 2024 (Figure 1d). This corresponds to an "extreme" G5 level of NOAA geomagnetic storm classification. The previous, pre-storm day of 9 May 2024 was very quiet with

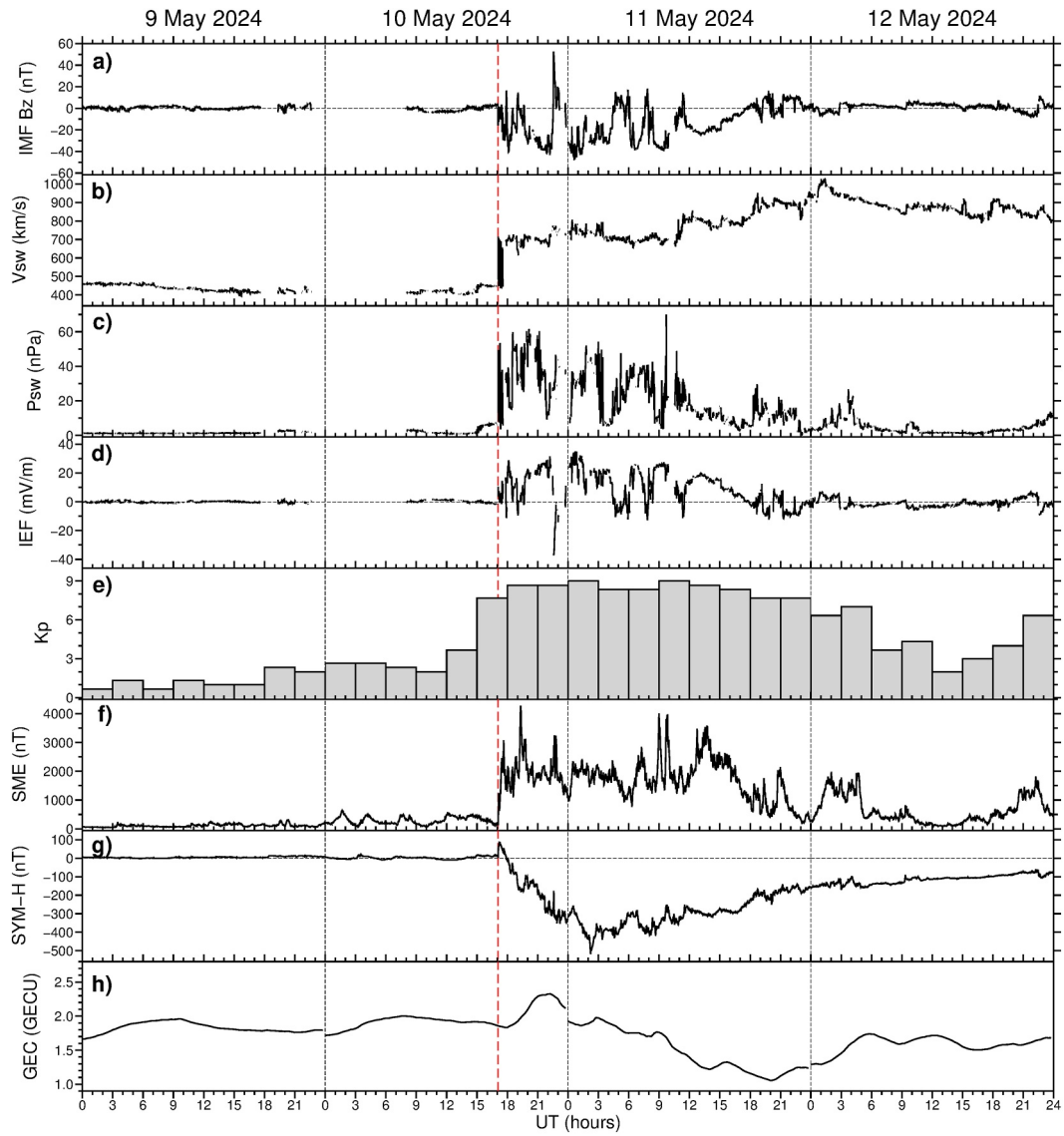

Figure 1. Geomagnetic conditions during 9–12 May 2024: (a) Interplanetary Magnetic Field (IMF) Bz component, (b) velocity and (c) dynamic pressure of the solar wind, (d) Interplanetary Electric Field (IEF), (e) Kp index, (f) SuperMAG auroral electrojet index SME, analog of AE, and (g) SYM-H index. The bottom panel (h) shows Global Electron Content (GEC) variations. The red dashed line shows storm commencement time.

the daily sum of Kp values of ∼10 only, whereas this value spiked to ∼38 and ∼67 for 10 May and 11 May, respectively.

The interplanetary magnetic field (IMF) north-south component Bz was near zero levels shortly before the SSC (Figure 1a). After that, it turned southward reaching −40.4 nT at 18:07 UT and then turned northward reaching +14 nT at 19:03 UT. The distinct large period of the steady southward IMF Bz was from 19:05 UT until 22:31 UT with the next minimum value of −43.4 nT at 22:12 UT. During that period of time, the interplanetary electric field (IEF) dawn-to-dusk component Ey, potentially associated with penetration electric fields to low latitudes, was steady positive with a maximum value of ∼20–26 mV/m (Figure 1d). The IMF Bz suddenly shifted northward to +52.5 nT at 22:34 UT. The next period of the steady southward IMF Bz was from 23:42 until 04:26 UT with the next minimum value of −47.85 nT at 00:36 UT.

Figure 1f shows variations of the SME (SuperMAG electrojet) index, a generalization of the auroral electrojet index calculated from 100+ sites instead of the 12 used in the official auroral electrojet indices like AE

(Gjerloev, 2012; Newell & Gjerloev, 2011). Shortly after the SSC, the SME index quickly surged to ∼2,500–3,000 nT and maintained at a consistently high level above 1,500–2,000 nT, with several significant spikes, for many hours until ∼17 UT on 11 May 2024.

In Figure 1g, the SYM-H index reflects the strength of the equatorial ring current and, as a result, the geomagnetic storm. During ∼10 min in the storm's initial phase, the SYM-H rose rapidly from the background level of ∼0–10 nT to +88 nT. After that, the SYM-H drops rapidly in several steps, first to a minimal value of −183 nT at 19:21 UT with the estimated change rate of ∼125 nT/hr, then to −354 nT at 23:12 UT, and the third decrease stage was from −257 nT at 00:30 UT to the minimum of −518 nT at 02:14 UT on 11 May 2024. The SYM-H rate change averaged during the entire main phase of the storm was of order −67 nT/hr. Thus, this storm was characterized by a 9-hr-long main phase, beginning around 17 UT on 10 May and ending around 02 UT on 11 May 2024. Starting at 02 UT on 11 May, the recovery phase went on for at least three days.

Figure 1h presents variations in Global Electron Content (GEC), calculated from 15-min Global Ionospheric Maps, for 9–12 May 2024. During the storm's main phase, from the onset until the end of the day of 10 May, the GEC experienced a significant surge by 20%–30% from the level of ∼1.8 GECU to ∼2.3 GECU, indicating the general increase of density in the entire Earth's ionosphere. It is an indirect sign that the storm caused not only the ionospheric plasma redistribution like poleward expansion of the equatorial ionization anomaly (EIA), but actually produced a notable increase of the ionospheric density on a global scale level, considering that GEC already includes all concurrent negative storm effects (large-scale density decreases due to recombination) on the night side of the Earth. On the next day of 11 May 2024, during in the recovery phase of the storm, the GEC demonstrates a long-lasting global ionospheric decrease to a level of ∼1 GECU, equivalent to a ∼40% total decrease from the normal conditions—a sign of predominance of the negative storm effects on a global scale during this recovery phase. The observed GEC behavior is also consistent with the storm profile of GEC changes outlined in Gulyaeva and Veselovsky (2012). Thus, the major storm-time increase of the ionosphere occurred primarily during the main phase of the May 2024 storm.

4. Results and Discussion

4.1. Ground-Based GNSS TEC

First, we examined an occurrence of large-scale ionospheric effects using ground-based GNSS TEC observations —specifically, high-resolution global TEC maps. Figure 2 shows global TEC maps from 17 UT to 03 UT for a pre-storm day (9 May 2024), storm day (10/11 May 2024), and TEC difference (storm vs. quiet), with a 2–hr interval. To facilitate comparison, TEC maps for both pre-storm and storm days utilized the same color scale. Figure 2a shows maps of TEC and TEC differences for 17 UT, shortly after a period when the SSC was just registered on 10 May 2024. The TEC maps for 9 May and 10 May 2024 exhibit a strong similarity, which is also indicated by the minimal TEC differences observed, even in the daytime equatorial sector. Usually, it takes about 2–3 hr after SSC for significant ionospheric TEC changes to develop and become noticeable (e.g., Lei et al., 2008; Wang et al., 2010). Figure 2b displays the TEC maps covering the next period of 19 UT. Here, we can start to notice the intensification of the EIA on 10 May 2024, with the EIA expanding toward higher latitudes in the American sector and prominent TEC enhancements at both EIA crests. The differential TEC map shows these enhancements up to 20–40 TECU over low to mid-latitudes in the American sector. Two hours later at 21 UT (Figure 2c), the storm-time TEC map reveals drastic ionospheric enhancements on the dayside ionosphere. Positive storm effects were observed at low and middle latitudes, with strong TEC enhancements at the EIA crests up to 200 TECU. The differential TEC map reveals significant enhancements of more than 50 TECU at the EIA crests in the sunlit sector, along with wide-spread enhancements covering all mid-latitudes across the American longitude sector. The most pronounced negative storm effects in the daytime sector started to appear along the geomagnetic equator over South America, as the trough between the EIA crests deepened during the storm-time EIA intensification. At 23 UT on 10 May 2024 (Figure 2d), positive storm effects further enhanced in the daytime ionosphere over the Pacific and American longitudinal sectors. In the American sector, the EIA crests showed greater separation, expanded far away from the magnetic equator, along with the large-scale enhancement, associated with the Storm-Enhanced Density (SED) phenomenon, covered low to mid-latitudes of North America. A narrow, elongated TEC enhancement was also observed near Canada's western coast, suggesting a further transformation of the SED to a Tongue-of-Ionization (TOI) structure at high latitudes (as also confirmed in Themens et al., 2024). The South America's equatorial region, currently shifting into the post-sunset sector,

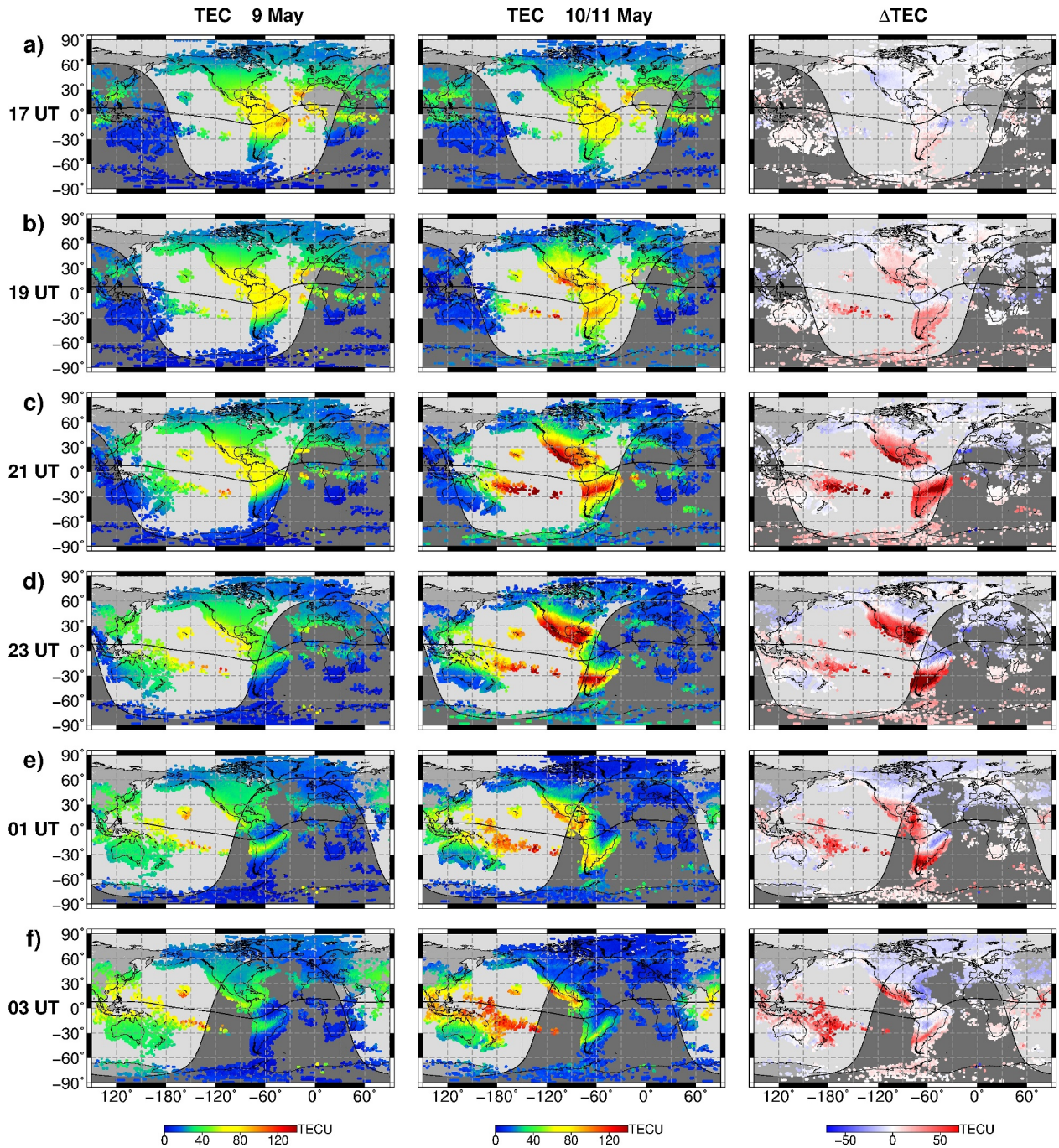

Figure 2. Ground-based GNSS TEC maps for (a–f) specific times from 17 UT to 03 UT for (left) quiet day of 9 May 2024 and (center) storm time on 10–11 May 2024, along with (right) corresponding TEC difference. The black line marks the magnetic equator, the shaded area shows terminator location and nighttime.

observed a significant and large-scale decrease in TEC. The differential TEC map (Figure 2d, right) clearly highlights the drastic positive storm effects at low and middle latitudes of both Americas, as well as the widespread negative storm effects over the geomagnetic equator in South America. At 01 UT on 11 May 2024 (Figure 2e), 2 hours later, we are still seeing an intensification of the EIA in the afternoon sector over the Pacific Ocean, notable TEC enhancements across low to middle latitudes mainly in the post-sunset period over North and South Americas, as well as a substantial TEC depletion over the magnetic equator region in South America. At 03 UT on 11 May 2024, the recovery phase of the storm just began. The TEC enhancements primarily took place at low latitudes in the Pacific and Asian sectors, which were sunlit (Figure 2f). The notable TEC enhancements in

the EIA crest regions remained present into the late evening across North and South Americas. More pronounced negative storm effects occurred at middle latitudes in North America and European sectors.

The overview of the global TEC maps demonstrates that during the storm's main phase from ~17 UT on 10 May 2024 until ~03 UT on 11 May 2024, the drastic TEC enhancements started to develop ~2 hr after the SSC and were associated with strong storm-time intensification of the EIA in the dayside ionosphere over the Pacific and American sectors (180°W–30°W). The most significant TEC enhancements were observed in the American sector, in terms of both magnitude and spatial extent.

4.2. Swarm Observations

Analysis of the ground-based TEC maps revealed the strong ionospheric response in terms of large-scale intensification of the EIA in the American and Pacific Ocean longitudinal sectors during the storm's main phase. Our examination of the EIA development and its full extent over the Pacific Ocean may be constrained due to the sparse ground-based data coverage in this water-dominated region. Fortunately, satellite observations can help us piece together a more detailed understanding of the changes in the ionosphere during this superstorm.

First, we analyzed in situ plasma density and topside TEC data from the three Swarm satellites. Figures 3a and 3b show a series of several consecutive overpasses of the Swarm A&C tandem with an equatorial crossing time of 19.1 LT and orbit altitude of ~475 km. The first overpass was near 12°E in central Africa during 17.7–18.3 UT, shortly after the storm onset. Observations of both in situ density and topside TEC are indicating the first signs of enhancements in the EIA crests (right plots of Figures 3a and 3b). The second overpass was over Western Africa at 19.3–19.9 UT. Here, in situ Ne density exhibited noticeable enhancements at both EIA crests, shifted poleward to much higher latitudes, and a deeper, wider EIA trough near the magnetic equator. Topside TEC data showed the EIA intensification above satellite orbit altitudes, and increased TEC over midlatitudes of the Northern Hemisphere. Third overpass was over the Atlantic Ocean near ~30°W longitude at 20.8–21.4 UT. In situ Ne density demonstrated a wide (~10° in latitude) and deep trough over the equator, along with a poleward shift and asymmetry in the EIA crests. Topside TEC values at the EIA crests reached ~70 TECU; this was ~3 times higher than quiet-time levels at northern locations, ~6 times higher at southern locations, and ~2.5 times higher than the quiet-time maximum near the magnetic equator. The lowest TEC value in the trough of the storm-time EIA exceeded the highest TEC value observed here during quiet time. The fourth overpass was near 53°W longitude in the American sector at 22.4–23.0 UT. Here, in situ Ne density data revealed a huge plasma density depletion near the equator, spanning more than 20° in latitude, with density in the EIA trough dropped to extremly low levels (under 10^4 el/cm^3). The observed effects are characteristic of the plasma "bite-out" phenomenon, where an extensive plasma density hole forms near the equator due to intense storm-driven upward plasma drifts, featuring very steep boundaries and a 2–3 order of magnitude density decrease (e.g., Abdu et al., 2005; Basu et al., 2001; Greenspan et al., 1991). Such dramatic decrease seen in the plasma density measurements is caused by the equatorial F layer rising to altitudes well above the satellite orbit (here, ~475 km).

At the same time, topside TEC observations indicate a dramatic amplification of both EIA crests in the topside ionosphere at altitudes above ~475 km (Figure 3b, pass #4). Both in situ density and TEC data show that the EIA structure displays asymmetry, with a significantly wider southern crest. The peak values in the EIA crests were ~3×10^6 el/cm^3, which is ~3 times greater than the crest values observed during quiet time conditions and ~4/20 times greater to the normal density level observed at north/south midlatitude locations where these crests shifted during the storm. In terms of TEC, the storm-time EIA enhancement reached ~83/104 TECU in the northern/southern crests, whereas no clear crests were observed in the topside TEC during quiet-time conditions with a general level of ~25 TECU near the equator and ~5–15 TECU at midlatitudes. So, the TEC enhancement in the EIA crests was at least 3–4 times higher than its quiet-time level. Here in the American sector, the EIA crest-to-crest distance reached around 60° in latitude, indicating an exceptional development of the EIA both in magnitude and poleward expansion.

The pass #5 was near 77°W longitude in the American sector at ~00 UT on 11 May 2024, both Swarm A and C satellites encountered another asymmetry in the EIA with a much larger and broader northern crest spanning over 30° in latitude across Central America. Here, the EIA crest-to-crest distance was ~40° in latitude, which is less than what was observed during the previous satellite pass. In the northern/southern crests of the EIA, the storm-time TEC enhancement reached around 104/68 TECU, showing a ~3 times increase from the quiet-time values. The ground-based TEC level was ~120 TECU here, meaning that topside TEC (above 500 km altitude)

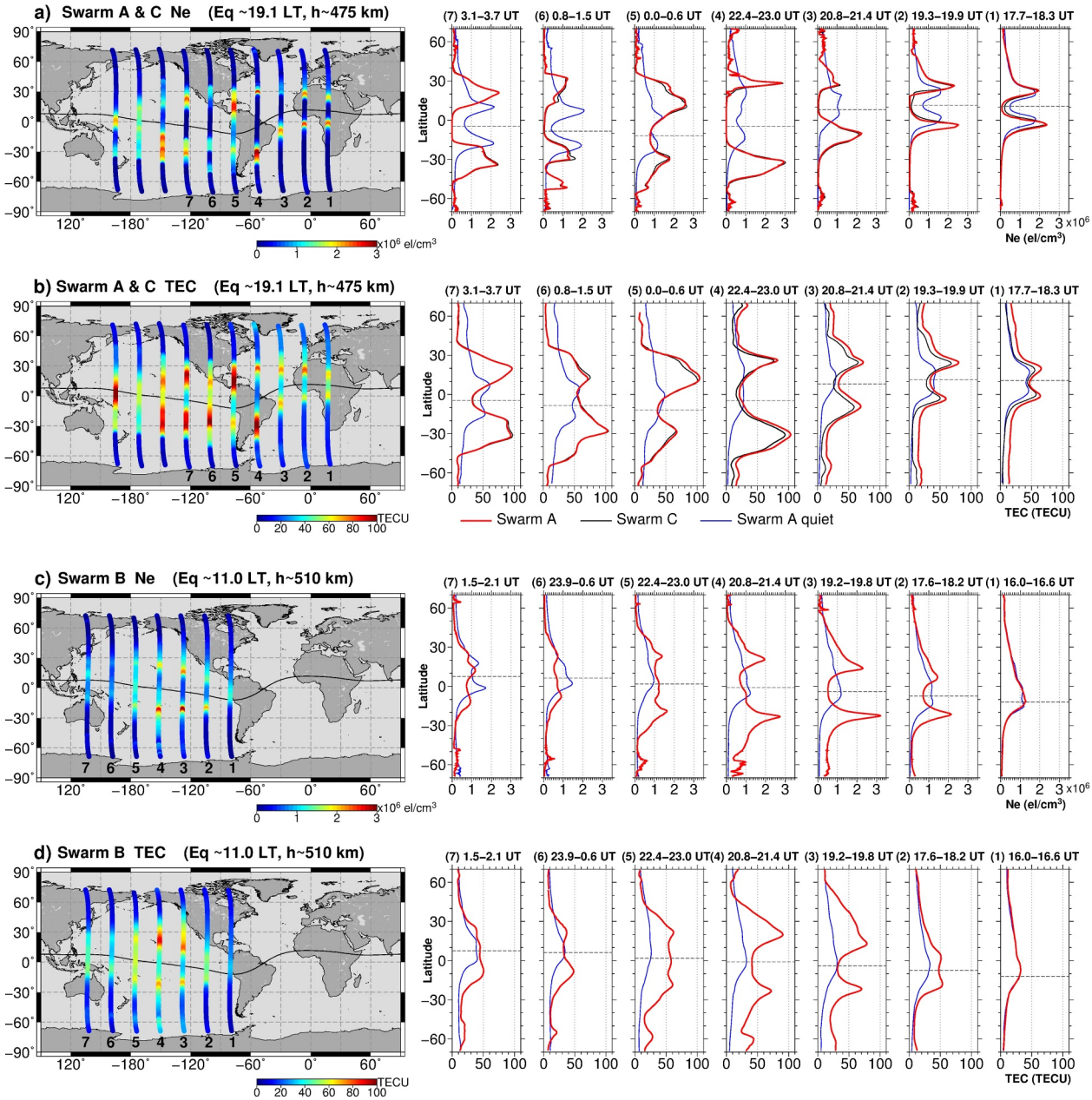

Figure 3. Swarm satellite observations of in situ electron density Ne and topside TEC plotted as a sequence of several consecutive overpasses on (left) geographical map and (right) separate panels for (a, b) a tandem of Swarm A & C and (c, d) upper Swarm B satellite during 10–11 May 2024. Each separate panel presents Swarm observations as a function of geographical latitude for the storm day (red curve) and previous quiet day (blue curve). The black curve represents Swarm C satellite observations, where available.

contributed ~85% to the ground-based value in the area of the northern EIA crest. Actually, this significant TEC enhancement in the Northern Hemisphere is clearly seen in the ground-based TEC maps after 21–23 UT on 10 May 2024 (Figures 2c and 2d, middle). This enhancement covers a large portion of Central and North Americas and is most likely related to the development of the SED in the American sector.

In the next passes, the in situ density observations indicate a poleward expansion of the EIA crests by ~20° toward higher latitudes, however their peak values were lower than those seen in previous satellite passes over the American sector, even approaching the quiet-time peak values. The topside TEC observations (Figure 3b, passes #6–7) showed much stronger effects, with the EIA crests exhibiting TEC enhancements up to ~100 TECU

(increase by 2–4 times to the quiet-time level) and a wide latitudinal separation of ∼40–50°. The EIA intensification with two distinct crests was detected to ∼150°W longitude in the Pacific Ocean and until ∼5–6 UT on 11 May 2024, shortly after the storm main phase ended and the IMF Bz turned northward near 05 UT (Figure 1a), suggesting ending of favorable conditions for prompt penetration electric fields (PPEFs).

The upper Swarm satellite, Swarm B, entered the American longitudinal sector shortly before the storm onset and then moved across longitudes in the Pacific Ocean (Figures 3c and 3d). The equatorial crossing time was ∼11 LT, so the satellite can observe the pre-noon formation of the EIA. During quiet-time conditions, the Swarm B observations indicate the absence of two-crest EIA structure, except for the pass #7 in the Australian sector, during pre-noon time at 11 LT in both in situ and topside TEC observations. This suggests that either the EIA was not well-developed or did not extend into the topside ionosphere above ∼500 km altitude. During the storm day of 10 May 2024, the pass #1 occurred at ∼80°W longitude in the American sector just prior to the storm onset. Both in situ and topside TEC observations exhibit remarkable similarity to the quiet-time conditions. After the storm onset, the Swarm B observations detected significant intensification of the EIA in the topside ionosphere above 500 km altitude. The EIA crests separation reached ∼35–45° in latitude in contrast to their absence in the quiet-time conditions. Even in this pre-noon early time sector, the peak values in the crests reached ∼2–3 × 10^6 el/cm^3, a level comparable to the evening-time EIA enhancements observed by Swarm A&C satellites. The topside TEC enhancements reached ∼70–90 TECU, while quiet-time values varied from ∼5 to 10 TECU at midlatitudes to ∼20–30 TECU at the equator. Topside TEC observations from passes #3–4 in Figure 3d also confirmed an extensive storm-time TEC enhancement covered a large area in the Northern Hemisphere between 10°N and 60°N during 19–22 UT on 10 May 2024. This ionospheric enhancement was much stronger in topside TEC than in in situ density observations. These signatures detected by the Swarm B satellite in the Pacific Ocean, specifically between 120°W and 150°W longitudes, are most likely a continuation of the large-scale SED-like structure detected in limited ground-based TEC observations over the North America sector (Figures 2c and 2d, middle).

4.3. GRACE-FO Observations

The three Swarm satellites provided observations of the storm-time EIA development at pre-noon (11 LT) and evening (19 LT) sectors. Another satellite mission, GRACE-FO, luckily had orbit passes in this region with an equatorial crossing time at ∼17 LT, allowing for insights into the after-noon sector. The GRACE-FO satellites had an orbit altitude around 490 km, rather similar to the Swarm mission. Figure 4 shows a series of several consecutive overpasses of GRACE-FO over the Atlantic-American-Pacific sectors, as well as KBR-derived in situ electron density and topside TEC observations along these passes. During 17–18 UT on 10 May 2024, shortly after the storm onset at 17:05 UT, the GRACE-FO observations exhibit identical behavior as in the control, quiet day (Figure 4, pass #1). The EIA started to experience a dramatic modification a few hours later, after 18–19 UT. The most significant density increases in the EIA crests occurred between 20 UT and 23 UT in the American sector (Figure 4, passes #3–4). At ∼22 UT (pass #4), the peak values in the EIA crests reached ∼3.5–4.1 × 10^6 el/cm^3, which is higher than the peak values in the crests observed here by Swarm at 19 LT (Figure 3a, pass #5). The EIA crests separation was ∼40° in latitude. Comparing the TEC levels, the topside TEC in the northern crest over Central America was approximately 117 TECU, whereas here, under quiet-time conditions, it was only around 25 TECU. The ground-based TEC over this area in Central America increased by two-fold to around 130 TECU, compared to the 55–60 TECU level during quiet-time conditions the day before. Therefore, the ground-based TEC values in the northern EIA crest were primarily influenced by the topside TEC, contributing approximately 85%–90%. Furthermore, a distinct hump in both density and topside TEC is seen poleward from the EIA crest, extending across low to midlatitudes (over 10–40°N) of the Northern Hemisphere, which can be associated with the TEC enhancement in the root zone of the SED-like structure discussed above.

Notably, the lack of a two-crest structure in topside TEC data from quiet-time satellite passes (#2–5, blue curves) over the American sector suggests that the EIA did not extend much above 500 km, even at ∼17 LT in the afternoon. During the storm's main phase, the EIA intensification led to a significant 2–6 times increase in topside TEC and the formation of two large peaks in the topside ionosphere (above 500 km altitude). As the GRACE-FO satellite progressed over the Pacific Ocean (Figure 4, passes #5–7), the topside TEC enhancements at middlatitudes were found to be much larger in the Southern Hemisphere. Therefore, in the Northern Hemisphere, a localized ionospheric enhancement at midlatitudes was largely confined to North and Central America only.

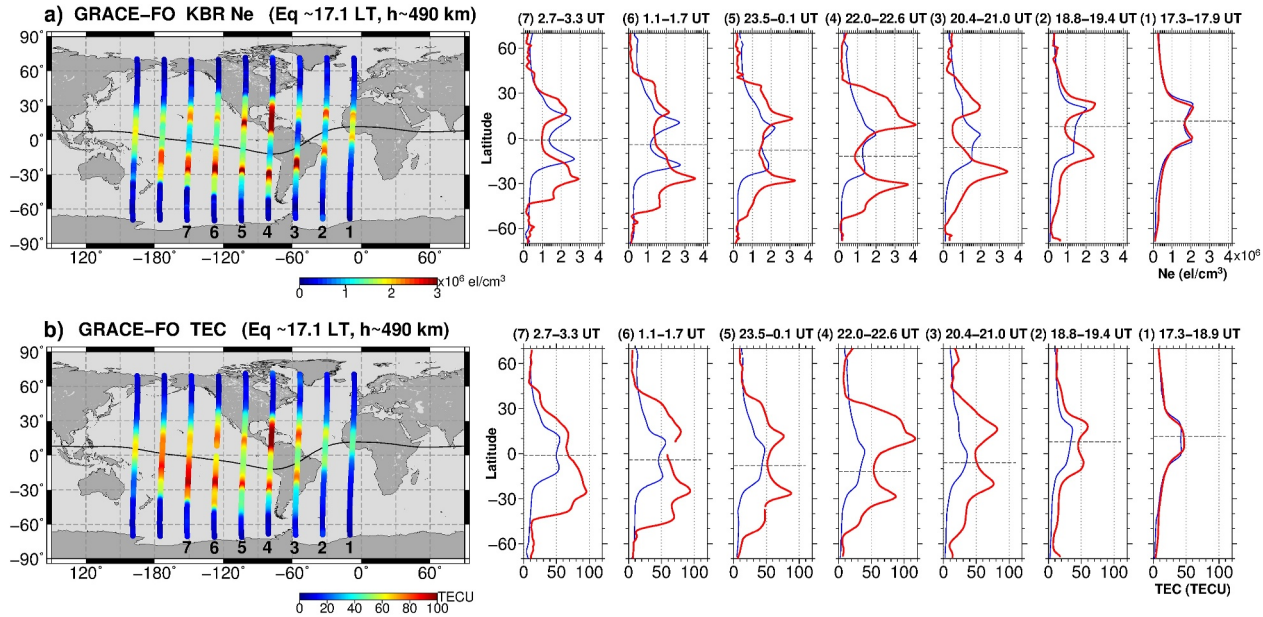

Figure 4. GRACE-FO satellite observations of (a) KBR-derived in situ electron density Ne and (b) topside TEC plotted as a sequence of several consecutive overpasses on (left) geographical map and (right) separate panels during 10–11 May 2024. Each separate panel presents GRACE-FO observations as a function of geographical latitude for storm day (red curve) and previous quiet day (blue curve).

4.4. COSMIC-2 Observations

For Swarm and GRACE-FO as polar-orbiting satellites, each successive orbit pass will cross the equator approximately ~20°–25° further west in longitude than the previous one (e.g., Figures 3 and 4), meaning no re-visiting of the same geographical area for at least the next 10–12 hr. This restricts the ability of a single polar orbiting satellite to provide information on how the ionosphere changes with time over a specific longitudinal sector. Did we possibly overlook much stronger effects of the storm-time EIA intensification due to specific limitations in the Swarm and GRACE-FO orbit configuration and available observational coverage on that particular storm day? Here, only satellites with low inclination orbits have the capability to sample equatorial and low latitude regions multiple times a day, allowing them to encounter repeatedly the same large-scale ionospheric structures, such as EIA crests.

Launched in 2019, the COSMIC-2 equatorial constellation represents the largest satellite-based observational system designed to study the equatorial ionosphere. By evenly distributing six satellites around the globe in a ~24° inclination orbit, the COSMIC-2 mission can effectively study the equatorial and low latitude ionosphere with a faster refresh rate than ever before. The COSMIC-2 satellites operated at ~525–550 km orbit altitude and provided observations of in situ ion density and topside TEC along their orbits. Six COSMIC-2 satellites are marked here as C2E1 to C2E6.

Figure 5 provides an overview of in situ density and topside TEC variability from each COSMIC-2 satellite during 9–11 May 2024. The plots are constructed as a function of geographical longitude and UT time to monitor ionospheric changes on an orbit-by-orbit basis. The presence of a brighter area at each orbit, which shifts noticeably as time progresses, indicates that the satellite encountered major ionospheric density/TEC enhancements in the equatorial ionosphere during local daytime (~12–16 LT) when the EIA becomes most developed with the largest values in its crests. It is important to note that when a satellite re-enters the same longitudinal zone, it can be at the different distance from the magnetic equator, for example, at the EIA crest or EIA trough, thus the recorded density level is highly dependent on a satellite location in the magnetic latitude (MLAT) domain. As shown in Figure 5, the most significant enhancements in both in situ density and topside TEC data over low latitude regions became noticeable after 17–18 UT on 10 May 2024. During the storm's main phase between 17 and 03 UT on 10–11 May 2024, significant ionospheric enhancements occurred over a broad range of longitude, specifically between 180°W and 30°W, most notably affecting the Pacific and American longitudinal sectors. Later in time, the zone of ionospheric enhancements moved further toward the sunlit Asian sector (120°–

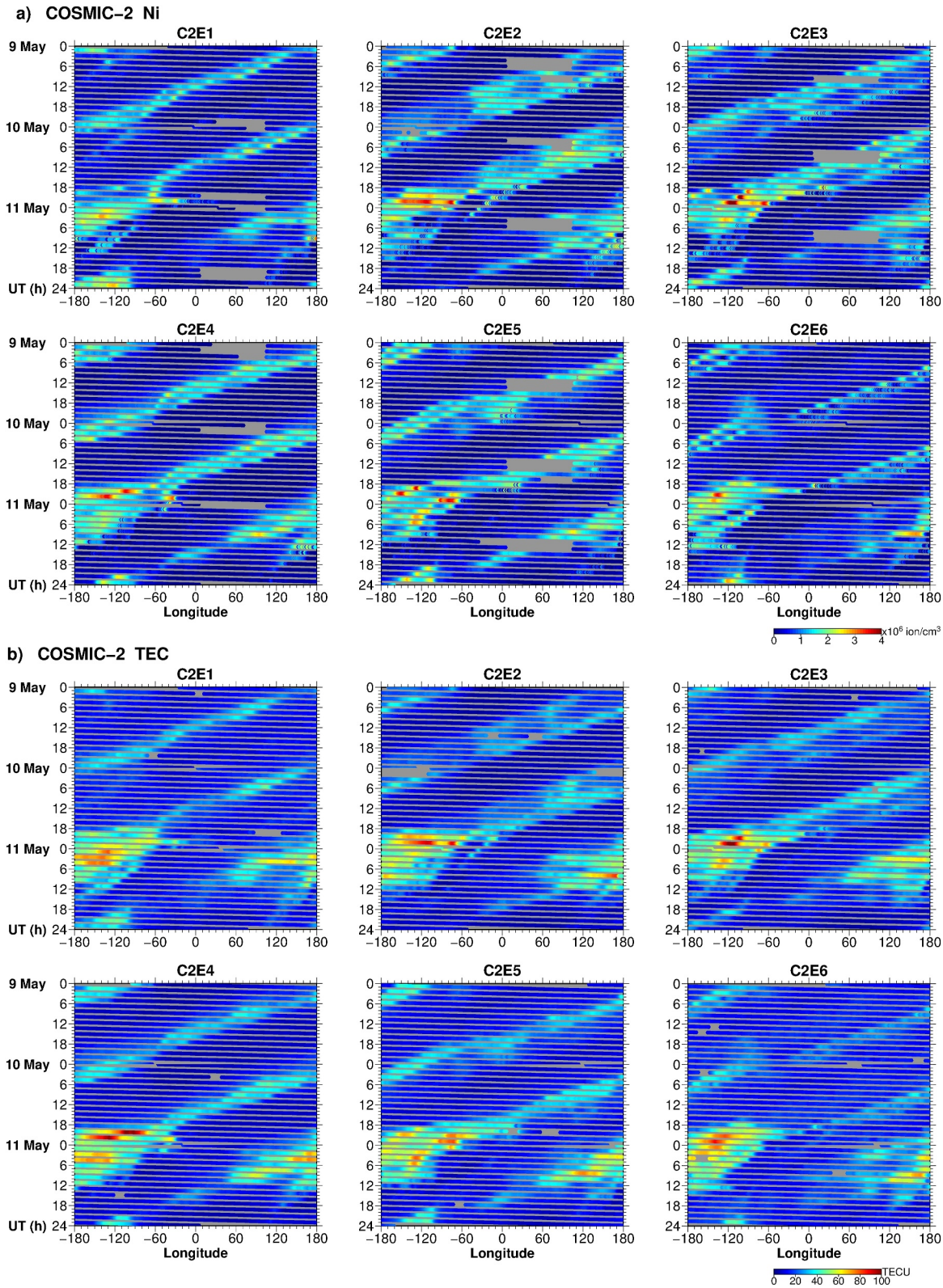

Figure 5. Observations of (a) in situ ion density Ni and (b) topside TEC for six COSMIC-2 satellites (C2E1–C2E6) plotted as a function of geographical longitude and UT time during 09–11 May 2024. Data gaps are indicated by the color gray. Satellites had ~525–550 km orbit altitude with low inclination (24°) in May 2024.

180°E). Thus, analysis of the data collected from six COSMIC-2 satellites covering the entire equatorial region clearly indicates that the most significant ionospheric enhancements during the storm's main phase were over the Pacific and American longitudinal sectors. These sectors were in daylight, the ionosphere was sunlit, and these effects related mainly to the storm-time intensification of the EIA due to super fountain effects.

Figure 6 provides a closer look at COSMIC-2 observations specifically whitin the American-Pacific sectors. Quiet-time conditions on individual plots are represented by dashed lines for reference. By examining topside TEC observations for altitudes above ∼535 km under quiet-time conditions, it is evident that mean values in the American sector (150°–30°W) ranged from ∼15 to ∼30 TECU (dashed lines in Figure 6, middle panels). Within a few hours after the storm onset, the topside TEC in this sector increased to ∼50 TECU (Figures 6a and 6b, middle panels). At 20–21 UT (Figure 6c), satellites C2E3 and C2E4 registered the topside TEC enhancements up to 86 and 98 TECU respectively over Central/North America near 13°N, 100°W. The increase is 3–4 times that of quiet-time conditions. At 21–22 UT (Figure 6d), two satellites C2E4 and C2E6 appeared quiet symmetrical to north and south of the magnetic equator over the Pacific. In the area spanning from 150°W to 110°W longitude, they observed the topside TEC enhancements up to ∼95 TECU in the north and ∼75–80 TECU in the south, at approximately 20° N/S MLAT.

At 22–23 UT (Figure 6e), satellite C2E6 re-appeared in a rather similar location south from the magnetic equator in the Pacific sector and still detected TEC increase of 75–85 TECU in this zone of ∼150°–120°W longitude. At that time, two other satellites, C2E2 and C2E3, were observed appearing to the north of the magnetic equator, above the Pacific Ocean just west of Central America. The C2E3 satellite detected a TEC enhancement of ∼100 TECU near 17°N, 115°W. Meanwhile, the C2E2 satellite, orbiting further north, encountered the same enhancement zone in its sloping part, measuring ∼90 TECU near 22°N, 110°W. Just eastward of North America closer to the sunset zone (60°–30°W in longitude), several COSMIC-2 satellites detected a rapid drop in TEC from ∼70 to 75 TECU level down to ∼15 TECU. These corresponds to a very deep depletion formed between EIA crests as a large-scale trough/hole in the evening sector seen in the ground-based TEC observations after ∼22 UT (e.g., Figure 2d, middle plot). The concurrent in situ ion density observations demonstrated a rapid drop of plasma density by several orders of magnitude from $\sim 3.5 \times 10^6$ ion/cm^3 to extremly low levels (under 10^4 ion/cm^3, approaching the lower limit of the IVM instrument sensitivity range) (Figure 6e, right plot). Such effects usually happens during storm-time plasma bite-outs, when the ionospheric F layer is uplifted above the equator to altitudes much higher than satellite orbits (here, ∼535 km).

The behavior of concurrent IVM ion density observations closely resembles that of topside TEC along the individual satellite passes (Figure 6, right panels). The largest ion density enhancements up to $\sim 4.6 \times 10^6$ ion/cm^3 were observed by the C2E3 satellite when it appeared near the zone of 10°–20°N, 120°–100°W, westward of Central/North America at 20–21 UT and 22–23 UT on 10 May 2024. These observations were made at around 25°N MLAT during conditions at approximately 14.2 LT and 15.2 LT. So far, these in situ density enhancements were the largest ones among those recorded by COSMIC-2, Swarm, and GRACE-FO satellites. We should mentioned that the rapid fluctuations in the IVM ion density data on the plots' right part related to the occurrence of equatorial plasma bubbles in the post-sunset period during both quiet-time and disturbed conditions.

4.5. Spire Observations

For this storm, we were fortunate to have topside TEC observations from multiple satellites of Spire's commercial mission. The orbit of several Spire satellites decreased near the end of their operational life, resulting in exceptional ionospheric observations from a remarkably low altitude. Figure 7 provides a summary of topside TEC observations from several Spire satellites, which crossed the American longitudinal sector during the main phase of the May 2024 storm.

Figure 7a presents results for Spire satellite S149, which was a polar-orbiting satellite with an orbit altitude lowered to ∼360 km altitude as of 10 May 2024. The equatorial crossing time was ∼11 LT. In quiet-time conditions, the topside TEC observations provided further evidence that there were no observable signs of a two-crest EIA structure forming and being detected in topside TEC data at ∼11 LT, even for altitudes above 360 km. It supports well the Swarm-B results made also for ∼11 LT but above ∼510 km altitudes (Figure 3d). So, in the quiet-time the EIA was not developed well at ∼11 LT. The first orbit corresponds to 17.5–18.1 UT, shortly after the storm onset, and we can see only minor intensification of EIA, primarily in the Southern Hemisphere. The second pass occurred after ∼19 UT near 126°W in the Pacific Ocean. Here, the strongly intensified EIA was

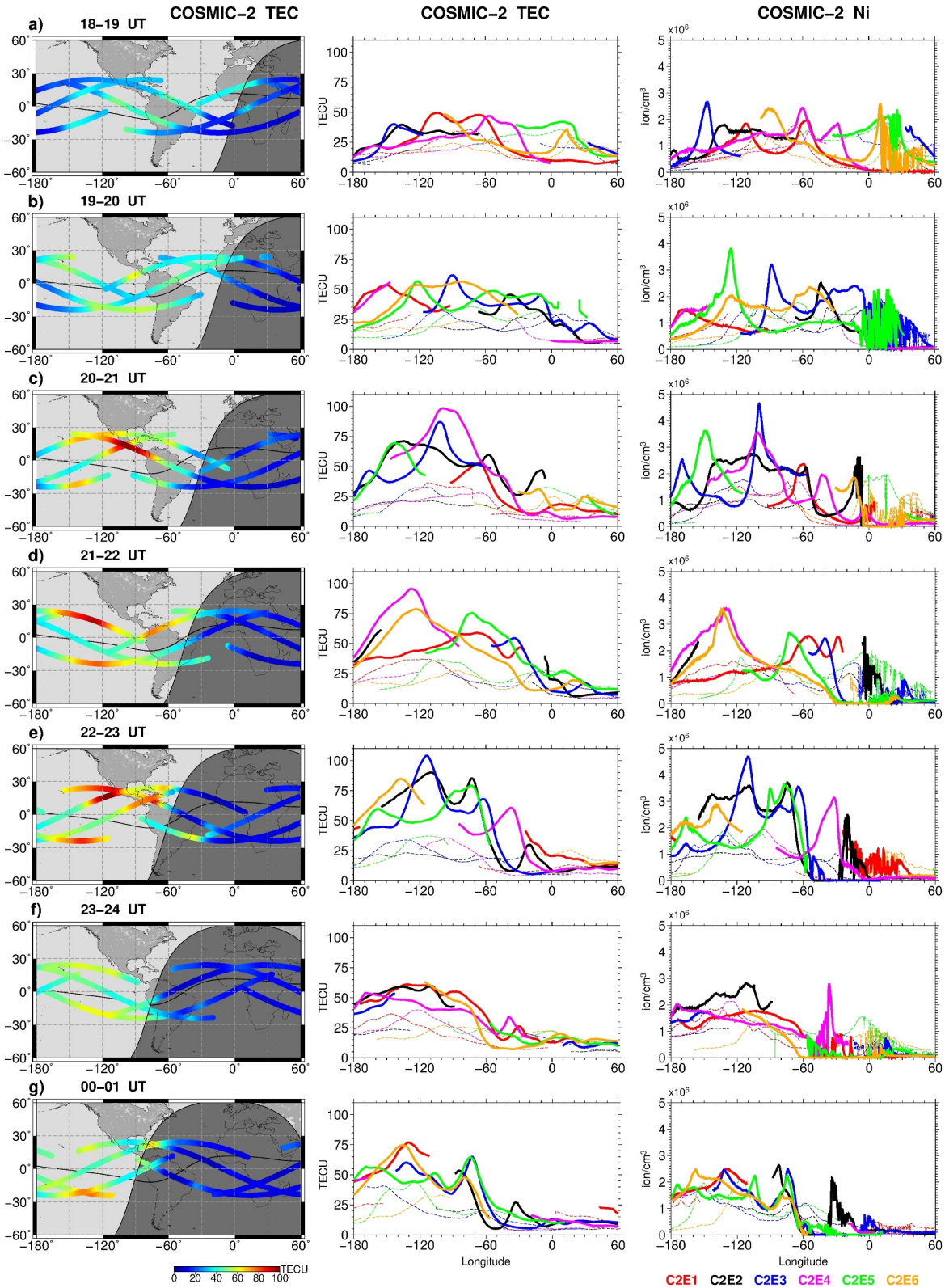

Figure 6. (a–g) Sequence of COSMIC-2 observations with focus on the American sector between 18 UT on 10 May 2024 and 01 UT on 11 May 2024. Each row shows geographical map with color-coded topside TEC observations along six COSMIC-2 satellite (C2E1–C2E6) tracks, and two separate panels with corresponding topside TEC and in situ ion density Ni data plotted as a function of geographical longitude. Dashed lines show TEC and Ni variations under quiet conditions for reference. The black line marks the magnetic equator, the shaded area shows terminator location and nighttime.

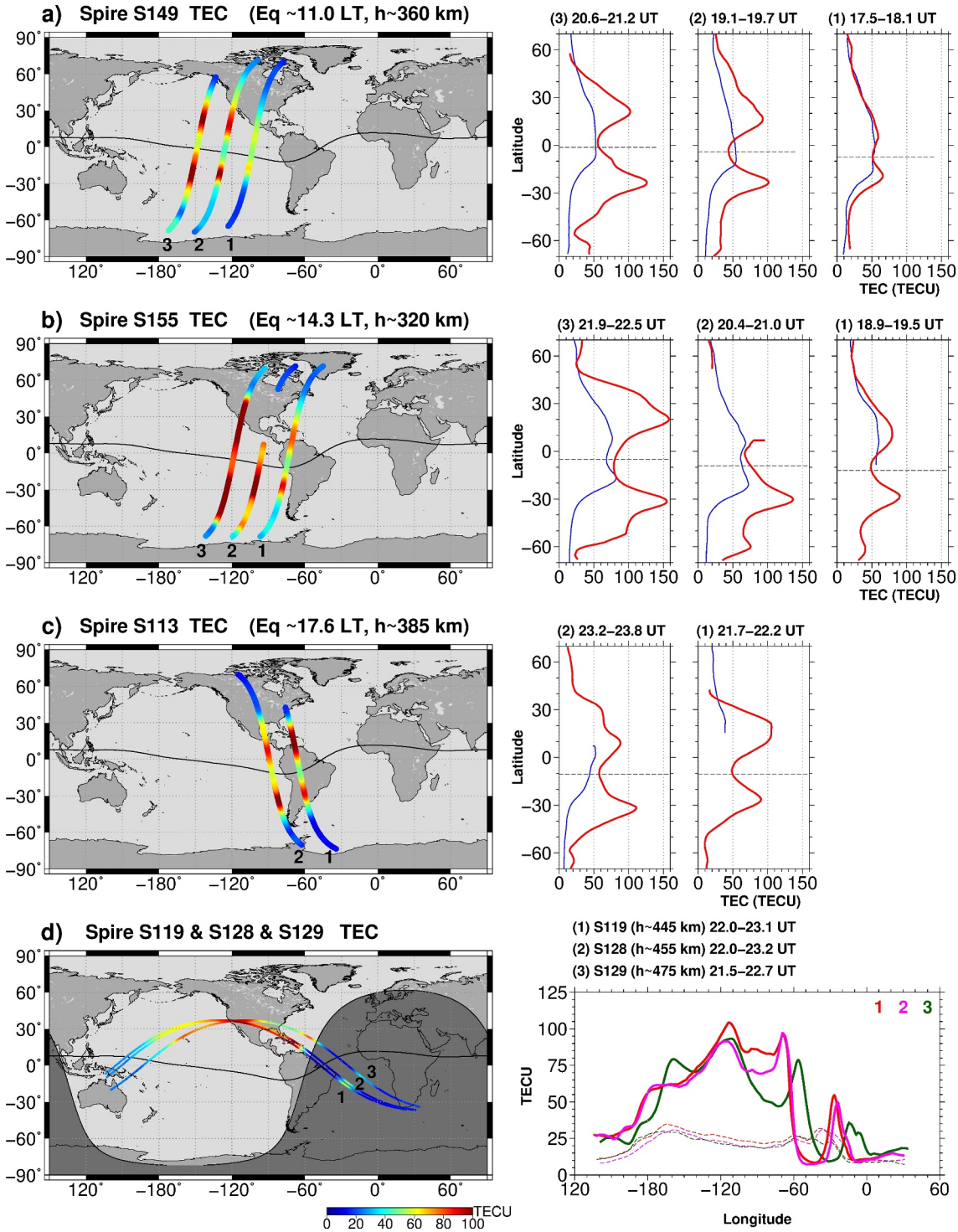

Figure 7. Spire satellite observations of topside TEC plotted as a sequence of several consecutive overpasses on (left) geographical map and (right) separate panels for (a) Spire S149, (b) Spire S155, (c) Spire S113, and (d) low-inclination-orbit Spire satellites S119, S128, and S129 during 10 May 2024. Quiet-time conditions on individual plots are represented by blue or dashed lines for reference.

detected with two well developed crests separated by ~40° in latitude. The peak values were 93 TECU for the northern EIA crest and 101 TECU for the southern crest. The third pass occurred at 20.6–21.2 UT near 148°W longitude over the Pacific Ocean. Here, the peak values reached 102 and 126 TECU for the northern and southern

EIA crests, respectively. The storm caused the topside TEC to rise to ∼2 times its quiet-time level in the Northern Hemisphere and ∼4–5 times in the Southern Hemisphere. The separation distance between EIA peaks reached ∼44° in latitude.

Figure 7b shows results for the S155 satellite, which was at an exceptionally low orbit of ∼320 km as of 10 May 2024. The equatorial crossing time, which was ∼14.3 LT, matches up well with the time when the EIA is expected to be most developed and should have its largest crest values. One can see a rapid response of the daytime EIA to the storm development. The first satellite pass occurred over South America (∼75°W) at ∼19 UT. The peak values of topside TEC in the EIA crests reached 80/90 TECU for the northern/southern EIA crests. During the second satellite pass at 20–21 UT, the peak value in the southern EIA crest increased to ∼135 TECU. At 22 UT, the third satellite pass crossed the equator near ∼120°W longitude and traversed across North America. Here, S155 registered a remarkable storm-time intensification of the EIA with topside TEC enhancements across a wide latitudinal range from 60°S to 50°N. The peak values reached 158 and 155 TECU for the northern and southern EIA crests, respectively. The observed crest values during the storm are approximately twice as large as those observed in the crests during quiet-time conditions, and two to four times larger than the normal density level at more poleward locations where these crests were displaced. The latitude separation between the EIA peaks was also very large, around 52°. Given that the ground-based TEC showed an increase to ∼190–200 TECU near the northern EIA crest during that period, the Spire S155 topside TEC observations reaching 158 TECU imply that the ionospheric density above ∼320 km altitude accounts for roughly 80% of the ground-based TEC.

So far, the S155 satellite detected the largest topside TEC enhancements in the EIA region over the American-Pacific sector compared to all other LEO missions, discussed in this paper. The key factors that led into this are: (a) the optimal LT when the EIA is most developed, and (b) the lowest orbit altitude (the vertical TEC above ∼320 km altitude should clearly exceed that above ∼500 km altitude). Additionaly, we need to note the existence of hump- or shoulder-like enhancements at midlatitudes in both the Northern and Southern Hemispheres, right after the EIA crest locations. It suggests that besides the strong eastward electric fields that uplift the equatorial ionosphere and greatly enhance the equatorial plasma fountain effects, leading to widespread EIA crests, other mechanisms such as storm-generated equatorward neutral winds also play a significant role in maintaining such enhanced density levels at higher latitudes.

Figure 7c presents results from Spire S113 satellite, which operated at an orbit altitude of ∼385 km and had the equatorial crossing time of ∼17.6 LT. As a result, it probed the EIA formation at a much later local time than the two preceding satellites. The first pass near 22 UT observed two large EIA crests of ∼106/90 TECU over South America, which were separated by ∼46° in latitude. The second pass at ∼23.5 UT observed a larger EIA crest of ∼111 TECU in the Southern Hemisphere and a smaller crest of ∼88 TECU in the Northern Hemisphere, separated by ∼41° in latitude. A shoulder-like TEC enhancement at ∼65–70 TECU level, located between 15°N and 40°N, was detected over North America, further poleward from the northern EIA crest. The observed feature matches closely with topside TEC observations from GRACE-FO, showing a similar shoulder-like structure at around 50 TECU level at the same time and in the same location over North America (Figure 4b, pass #5). Difference in absolute TEC values may result from the ionospheric contribution between orbit altitudes, as orbits were at ∼385 km for S113 and ∼490 km for GRACE-FO. This low to midlatitude enhancement most probably related to SED formation over North America during the storm's main phase.

Additionally, in Figure 7d, we show topside TEC data from three Spire satellites (S119, S128, and S129) in low-inclination orbits (37°) during their passage over the American sector within the same time window (21.5–23.0 UT) on 10 May 2024. They had orbit altitudes that were fairly close together, ranging from 445 to 475 km. Due to a much higher orbit inclination, these Spire satellites traversed over North America in a more northerly path compared to the COSMIC-2 satellites at that time window (Figure 6e). The Spire TEC observations demonstrate a high degree of similarities both in shape and magnitude to the COSMIC-2 TEC observations.

Here, COSMIC-2 satellites (∼535 km orbit altitude) detected the largest TEC enhancements of ∼100 TECU near 17°N, 115°W and ∼90 TECU further poleward near 22°N, 110°W. The lowest Spire S119 satellite registered a TEC enhancement of ∼104 TECU near 35°N, 115°W. Two other satellites S128 and S129 observed a similar TEC enhancement of ∼90–93 TECU over ∼35–37°N, 120°W–110°W. These detections located roughly 15° northward from COSMIC-2 observations and align well with a largely extended zone of elevated TEC observed over North America in ground-based GNSS data (Figures 2c and 2d). The registered topside TEC enhancements contribute by 60%–70% to the ground-based TEC values observed here at midlatitudes of North America. Near

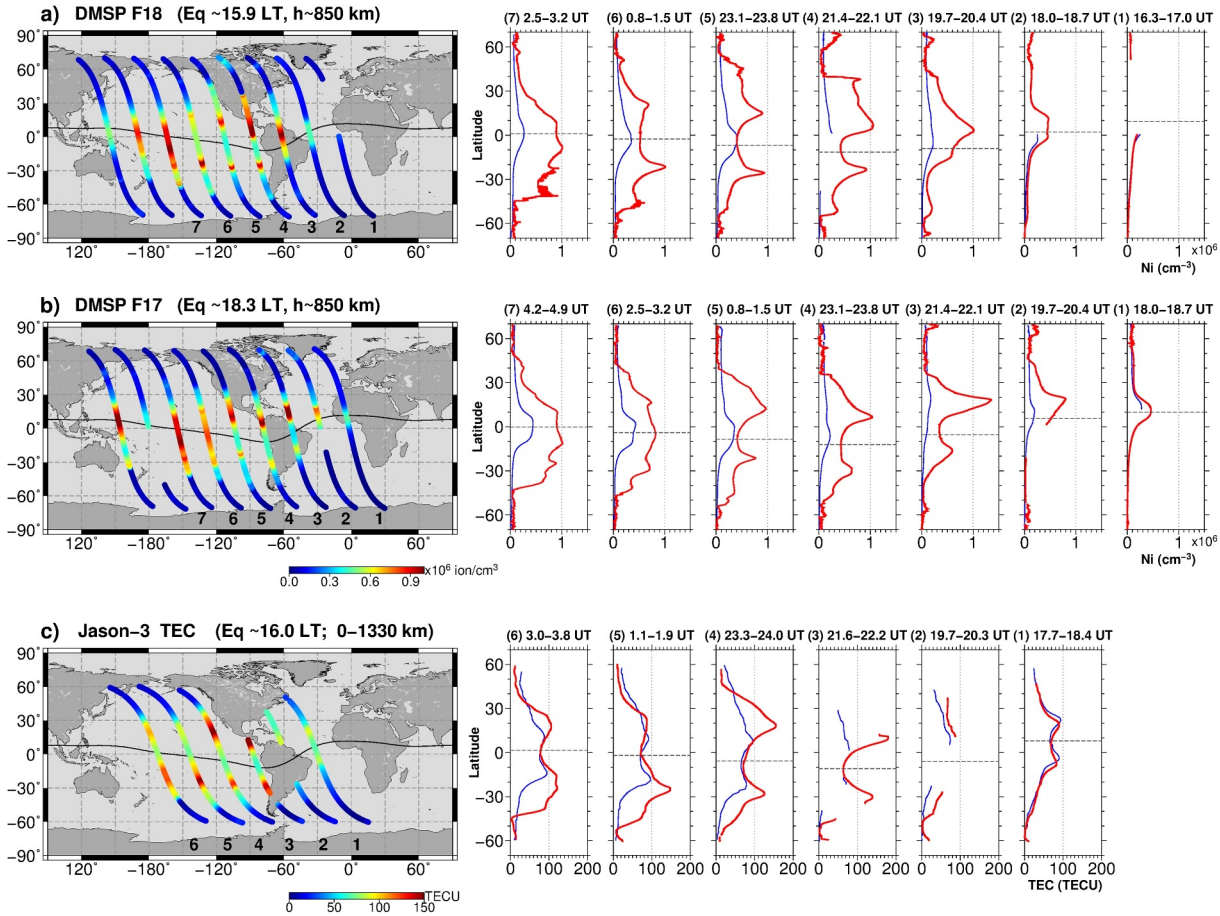

Figure 8. High-altitude satellite observations plotted as a sequence of several consecutive overpasses on (left) geographical map and (right) separate panels for in situ ion density at ~850-km altitude for (a) DMSP F–18 and (b) DMSP F–17 satellites, and (c) downward-looking TEC (0–1,330 km) for Jason–3 satellite during 10–11 May 2024. Each separate panel presents satellite observations as a function of geographical latitude for storm day (red curve) and previous quiet day (blue curve).

60°–20°W longitudes, all three satellites traversed through the large-scale plasma hole between evening-time EIA crests, registering an ubrupt drop in TEC. While passing over South America in close orbit tracks, both S119 and S128 satellites registered a significant drop (~10 times) in TEC from ~95 TECU to ~8 TECU over a short longitudinal distance (~10°). Such TEC drops within this plasma hole over the magnetic equator in South America were also detected by several COSMIC-2 satellites (Figure 6e). However, the Spire data very clearly detected the southern wall of this large-scale hole/trough. That strengthens the conclusion that the observed ionospheric decrese is a very localized depletion/bite-out, featuring distinct steep walls at both sides from the equator, and not a gradual TEC/density decrease at night side.

4.6. High Altitude Satellites: DMSP and Jason-3

Further, we analyzed available ionospheric observations collected by LEO satellites at significantly higher orbit altitudes, specifically DMSP and Jason-3. Figures 8a and 8b present in situ ion density observations registered along ~850 km orbit altitude by DMSP F18 and F17 satellites, respectively. Satellite F18 with the equatorial crossing time of ~15.9 LT traversed over the American-Pacific sector first. The observations under quiet-time conditions demonstrate a single-peak near the magnetic equator with modest maximal values of ~0.2–0.4 $\times 10^6$ ion/cm^3. The first strong effects started to be observed after ~19–20 UT. The in situ plasma density at that high altitude increased drastically to ~1.0 $\times 10^6$ ion/cm^3, reaching around 5 times the quiet-time level of ~0.2 $\times 10^6$ ion/cm^3, over the northern part of South America (Figure 8a, pass #3). At 21–22 UT along pass #4, satellite F18 encountered two distinct crests of the EIA at ~1.05/0.92 $\times 10^6$ ion/cm^3 level, as well as a shoulder-like density enhancement spanning across 10°N–40°N in North America. That suggests that this enhancement,

which is most likely related to the SED formation in this region and detected in topside TEC by several lower LEO satellites, extended well to much higher ionospheric/plasmaspheric altitudes even over North America mid-latitudes. After ~23 UT (Figure 8a, pass #5), satellite F18 continued to observe a remarkable expansion of the daytime EIA reaching up to $\sim 0.9 \times 10^6$ ion/cm^3 in the crests, that represent ~4 times increase from the quiet-time level for location of the northern EIA crest and ~8 times increase for the southern EIA crest. The separation between northern and southern EIA crests as detected at ~850 km altitude increased from ~31° at pass #4–~41° at pass #5.

DMSP F17 satellite with a later equatorial crossing time of ~18.3 LT appeared over the same region with the closely located orbit tracks, but approximately 1.5 hr after F18. Figure 8b shows that at ~22 UT along the pass #3, the satellite F17 passed through the same structure close to the northern part of South America as F18 did at ~20 UT. It detects that this single northern peak already reaching $\sim 1.0 \times 10^6$ ion/cm^3, two hours ago, transformed further into a more asymmetrical two-peak EIA structure with the northern crest dominating and reaching an impressive peak level of $\sim 1.35 \times 10^6$ ion/cm^3, that represent ~8 times increase from the quiet-time level. This particular region most probably related to the root region of the SED formation in the North American sector. During passes #4–5, satellite F17 further detected signatures of the two-peak EIA structure with a much stronger northern crest, as well as a zone of significant denisty enhancement that extended toward midlatitudes (up to ~40°N) over North America. While moving further into the Pacific Ocean from the west coast of North America during passes #6–7, both satellites F17 and F18 continued to observe a significant increase in ion plasma density at ~850 km altitudes across a latitudinal range of 40°S–40°N, with midlatitude enhancements becoming more prevalent in the Southern Hemisphere.

In contrast to satellite observations of up-looking topside TEC (above satellite orbits) discussed earlier, Figure 8c presents observations of downward-looking TEC provided by the Jason-3 altimeter mission below its orbit altitude. It is important to mention that Jason–3 downward-looking TEC (0–1,330 km) can be measured over water surface only, so gaps occurred when the satellite passed over land/continents. With the equatorial crossing time of ~16 LT, the satellite is expected to observe a well-developed daytime EIA while measuring the entire ionospheric electon content across 0–1,330 km altitudes. During pass #1 within ~1.5 hr of the storm onset, the satellite overflied the Atlantic sector and observed a two-peak EIA structure, very similar to a quiet-time behavior with maximal values of ~90 TECU and the peaks separation of ~25° in latitude. Later on, satellite overflied the American continents and had data gaps in observation records. Partial data from pass #3 at ~22 UT reveals a significant intensification of the EIA just west of South America. Peak values of up to 180/140 TECU are observed in the northern/southern EIA crests, with a latitudinal separation of approximately 40°. Here, in the vicinity of the northern EIA crest near 100°W, the ground-based TEC indicated an enhancement level of ~190–200 TECU. During pass #4, the satellite registered a well intensified EIA with peaks up to 155/125 TECU in the northern/southern crests, with a much larger latitudinal separation of ~47°. With respect to the EIA peak values of ~96/79 TECU in the previous quiet day, the storm-time increase in the peaks itself was only ~1.6 times (~60%). However, the peak increase reached 2 times and more when comparing to the quiet-time values at locations where the peaks were moved. Also, the minimum observed at the EIA trough over the magnetic equator was ~70 TECU, similar to the quiet day, indicating that most significant changes occurred specifically at low to middle latitudes of both hemispheres, where EIA crests shifted. It suggests that even in the daytime region with a fully developed EIA (16 LT), the absolute values of the ionospheric TEC (0–1,330 km) did not undergo drastic changes (only ~1.6 times in the peaks) and major effects were registered due to changes in the vertical density redistrubution (e.g., multifold increases in topside density and topside TEC) and in the meridional density redistribution (e.g., EIA crests shifting to more poleward positions).

4.7. An Integrated Overview on the Storm-Time Reaction of the Equatorial Ionization Anomaly in the American/Pacific Sector

The analysis of ionospheric observations from multiple LEO satellite observations revealed that during the main phase of the storm, the most prominent ionospheric enhancements occurred specifically in the American/Pacific longitudinal sectors. In Table 1, we summarized the key characteristics of the observed storm-time EIA enhancements. As we analyzed multiple missions with remote sensing (GNSS TEC) and in-situ plasma probe observations, this table was divided into two corresponding sections. For topside TEC, measured above a satellite orbit, we include three Spire polar-orbiting satellites operated at altitudes between 320 and 385 km, Swarm A at ~475 km, GRACE-FO at ~490, Swarm B at ~510 km. We also included downward-looking TEC observation

Table 1
Summary Table of the Storm-Time EIA Enhancement in the American/Pacific Sector as Derived From Multiple LEO Satellite Observations

LEO	Altitude	UT (LT)	Longitude	Max in north/south crests	Min in trough	Crest-to-trough ratio	Crest-to-crest distance
TEC				TECU	TECU		
Spire S155	>320 km	22.2 (14.3)	120°W	**158**/155	79	2.0	**52°**
Spire S149	>360 km	19.3 (11.0)	126°W	93/101	**44**	**2.3**	40°
	>360 km	20.8 (11.0)	148°W	102/**126**	56	2.2	44°
Spire S113	>385 km	22.0 (17.6)	65°W	**106**/90	49	**2.2**	**46°**
	>385 km	23.5 (17.6)	87°W	88/111	58	1.9	41°
Swarm A	>475 km	21.1 (19.1)	30°W	73/69	33	2.2	34°
	>475 km	22.7 (19.1)	53°W	83/**104**	**21**	**4.9**	**57°**
	>475 km	0.3 (19.1)	77°W	**104**/68	36	2.8	41°
GRACE-FO	>490 km	20.7 (17.1)	55°W	82/77	48	1.7	36°
	>490 km	22.4 (17.1)	80°W	**117**/87	53	**2.2**	**39°**
	>490 km	23.9 (17.1)	103°W	77/87	**51**	1.7	38°
Swarm B	>510 km	19.5 (11.0)	128°W	79/70	**31**	**2.5**	35°
	>510 km	21.0 (11.0)	151°W	**90**/72	41	2.2	**43°**
Jason-3	0–1,330 km	21.7 (16.0)	91°W	**180**/139	**63**	**2.8**	40°
	0–1,330 km	23.7 (16.0)	112°W	155/125	70	2.2	**47°**
Ground TEC	0–20,000 km	23.0	75°W	133/141	48	2.9	54°
In situ density				$\times 10^6$ cm^{-3}	$\times 10^6$ cm^{-3}		
Swarm A	@475 km	21.1 (19.1)	30°W	1.05/2.24	**0.03**	**74.9**	38°
	@475 km	22.7 (19.1)	53°W	2.87/**2.94**	**0.006**	**511.0**	**60°**
	@475 km	0.3 (19.1)	77°W	2.59/1.78	0.78	3.3	42°
GRACE-FO	@490 km	20.7 (17.1)	55°W	1.95/3.39	**0.48**	**7.0**	**43°**
	@490 km	22.4 (17.1)	80°W	**4.10**/3.69	0.87	4.7	40°
	@490 km	23.9 (17.1)	103°W	3.13/3.27	1.37	2.3	41°
Swarm B	@510 km	19.5 (11.0)	128°W	2.30/**3.19**	**0.52**	**6.1**	36°
	@510 km	21.0 (11.0)	151°W	1.95/2.73	0.68	4.0	**44°**
DMSP F18	@850 km	21.7 (15.9)	85°W	**1.05**/0.92	0.42	2.5	31°
	@850 km	23.4 (15.9)	111°W	0.90/0.93	**0.40**	2.3	**41°**
DMSP F17	@850 km	21.8 (18.3)	52°W	**1.35**/0.59	**0.34**	**4.0**	35°
	@850 km	23.4 (18.3)	75°W	1.03/0.64	0.43	2.0	**36°**
	@850 km	1.1 (18.3)	102°W	0.97/0.77	0.41	2.3	34°

Note. The largest values for each satellite mission are shown in bold.

from the Jason-3 satellite orbiting at ∼1,330 km and full-range TEC from ground level up to ∼20,000 km altitude. For in-situ density measurements along satellite orbits, we include plasma density values from Swarm A and B spacecrafts, GRACE-FO, and higher-orbit satellites DMSP F17 and F18 at an altitude of ∼850 km.

For topside TEC, the largest values in the EIA crests up to 158/155 TECU were registered by the lowest orbiting satellite from the considered set, Spire S155 at ∼320 km altitude, near 22.2 UT (∼14.3 LT) on 10 May 2024. Other satellites registered the EIA enhancements in the crests mostly within the range between 70 and 100 TECU, which was quite significant given that the quiet-time level was primarily ∼30 TECU. During the main phase of the storm, the enhanced fountain effect resulted in a wider separation of the EIA crests as they shifted further poleward from the magnetic equator. These high-inclination-orbit satellites registered the EIA crest-to-crest distance mostly between 34° and 46° in latitude. The largest crests separation of 52° and 57° was observed again by the lowest Spire S155 satellite at ∼22.1 UT (∼14 LT) near 120°W longitude in the Pacific Ocean and by the Swarm A satellite at ∼22.7 UT (∼19 LT) near 53°W over South America/Brazil. The first satellite overflied

the daytime EIA at its most developed state, while the second one encountered the evening sector near sunset, where eastward PPEFs can greatly enhance effects of the pre-reversal enhancement (PRE) of zonal electric fields. At that particular time, the conditions were remarkably favorable for PPEFs, coinciding with a prolonged period of a steady southward IMF Bz from ∼19 until 22:31 UT with the minimum value of −43.4 nT recorded at 22:12 UT (Figure 1a). During that time, LEO satellites observed the most prominent EIA enhancement effects in different sections of the EIA. The crest-to-trough ratio of the enhanced EIA ranged mainly between 1.7 and 2.2. The largest ratio value of 4.9 was detected along the discussed pass of Swarm A satellite at ∼22.7 UT (∼19 LT) near 53°W. Besides the higher values in the EIA crests and increased cres-to-crest separation, the EIA trough experiences here a decrease to ∼21 TECU, marking the lowest trough value recorded in this part of the table. This indicates the presence of strong $\mathbf{E} \times \mathbf{B}$ drifts and active conditions for fountain effects in the evening sector over South America. Jason-3 satellite, measuring the entire ionospheric content between 0 and 1,330 km, registered largest TEC enhhancements in the crests up to 150–180 TECU, the crest-to-trough ratio of rather similar level of 2.2 and 2.8, as well as the EIA crests separation up to 40°–47° in latitude for conditions of ∼16 LT. The ground-based TEC is provided here for ∼75°W longitude, where we have observations of EIA crests and trough structures in both hemispheres. Around 23 UT in the American sector, the ground-based TEC showed a crest-to-trough ratio of 2.9 and an EIA crests separation of 54° latitude, which are quite consistent with satellite observations.

Results from in-situ plasma density observations indicate similar patterns in the EIA enhancements as topside TEC. The observed EIA crest-to-crest distance ranged between 31° and 44° in latitude. The largest separation of 60° was observed along the same pass of Swarm A satellite at ∼22.7 UT (∼19 LT) near 53°W over South America, where crests separation in topside TEC was ∼57° in latitudes, the largest one too. Along this pass, the crest-to-trough ratio has an extreeme value of 511. That occurred due to the density drop in the trough region to an extremely low level, indicating plasma bite-out conditions, when strong equatorial plasma fountain uplifted ionospheric plasma to much higher altitudes than the Swarm A satellite orbit (∼475 km) with further downward plasma diffusion forming more poleward EIA crests. Plasma bite-out conditions near the magnetic equator can explain the very low values ∼21 TECU observed simultaneously in topside TEC within the EIA trough. For all other satellites orbiting at ∼500 km altitude, the distance between crests was about 40° and the crest-to-trough ratio varied from 2 to 7. For DMSP satellites orbiting at ∼850 km altitude, the distance between crests was 31°–41° in latitude and the crest-to-trough ratio varied from 2 to 4. Regarding the largest absolute values observed in in situ density, the peak values of $4.1/3.7 \times 10^6$ el/cm^3 were registered along the GRACE-FO pass at ∼490 km altitude near 80°W in the American sector at 22.4 UT (17.1 LT).

These values surpassed the density level of $\sim 2.9 \times 10^6$ el/cm^3 observed near the same time in the dusk sector by Swarm A satellite, when the largest EIA crests separation was registered. Also, topside TEC observations along this GRACE-FO pass were higher compared to those during the Swarm A pass (117/87 TECU vs. 83/104 TECU, respectively). That indicates that values in the EIA crests corresponded to the topside ionosphere were larger during ∼17 LT than those observed at ∼19 LT, even under conditions of strongly intensified equatorial plasma fountain. The lowest Spire S155 satellite recorded the largest topside TEC values of 158/155 TECU near the same time at ∼14.3 LT sector, further affirming this fact. Minimal density levels recorded in the EIA trough and abnormal crest-to-trough ratios demonstrate that plasma bite-out conditions were observed along several Swarm A overpasses only.

In Figure 9, there is a summary plot that demonstrates the EIA crest detections in space-based TEC observations from different missions, showing the relationship with local time and geographic longitude. Figure 9a shows the TEC peak values in the EIA crests as a function of magnetic latitude and local time. We have multiple satellite observations covering the daytime sector from 10 LT to 20 LT, matching the expected time for the EIA to form and fully develop. The storm-time EIA peaks were predominantly spotted close to 20° MLAT, specifically between 18° and 23°, in both hemispheres and consistently across all considered local times. The most poleward expansion of EIA crests up to 25°–27° MLAT were detected between 19 and 20 LT, which could be attributed to the superposition of eastward PPEFs on PRE fields near the dusk sector. Figure 9b presents the same observational data set but plotted as a function of MLAT and geographic longitude. It is rather evident that poleward expansion of the EIA crests to near the same 20°MLAT level occurred in various longitudes spanning from the Pacific to American sectors. This largest expansion up to 25°–27° MLAT was detected at 50°–60°W longitudes in South America.

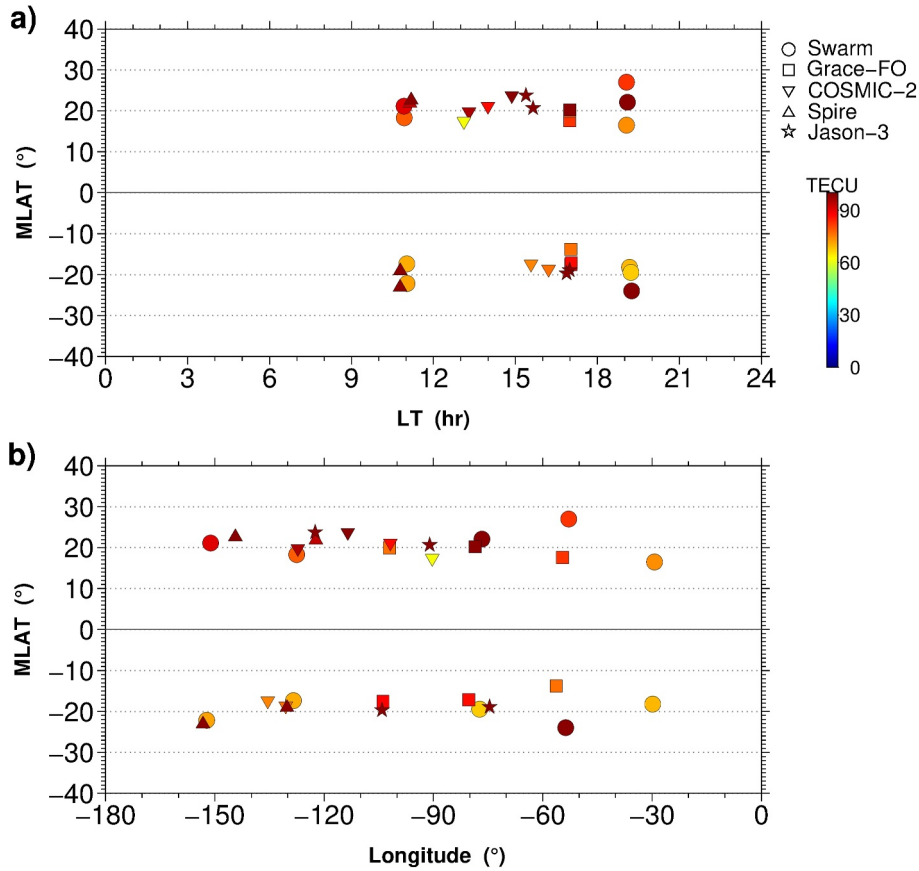

Figure 9. Meridional expansion of the EIA crests in terms of magnetic latitude (MLAT), plotted as a function of (a) local time (LT) and (b) geographic longitude, during the main phase of the storm. Symbols represent various LEO missions, while colors represent the observed TEC value.

5. Summary

We investigated the global ionospheric response during the main phase of the 10–11 May 2024 geomagnetic storm using a comprehensive set of 20 LEO satellites that operate at orbit altitudes between 320 and 1,330 km and provide ionospheric observations like in situ plasma density or TEC. The main findings of this study can be outlined as follows:

1. The global maps of ground-based TEC demonstrates that during the storm's main phase (17–03 UT) the drastic TEC enhancements started to develop ∼2 hr after the SSC and were associated with strong storm-time intensification of the EIA in the dayside ionosphere over the Pacific and American sectors. The ground-based TEC increased to ∼200 TECU. The most significant TEC enhancements were observed in the American longitude sector, in terms of both magnitude and spatial extent toward middle latitudes.
2. Data from six evenly spaced COSMIC-2 satellites, which continuously monitor the equatorial ionosphere around the globe, revealed that the most significant ionospheric enhancements during the storm's main phase occurred predominantly between 180°W and 30°W in the Pacific and American longitudinal sectors, which were in daylight.
3. As detected by multiple satellites, the crests of the storm-enhanced EIA expanded poleward to ∼18°–23° MLAT and remained consistent near this level across different local times (10–20 LT). However the largest EIA expansion with crests reaching 25°–27° MLAT in both hemispheres was detected between 19 and 20 LT, which could be attributed to the superposition of eastward PPEFs on PRE fields near the dusk sector. Specifically, this largest expansion was detected at 50°–60°W longitudes in South America. Under the quiet conditions, the EIA crests located near usual 10°–15° MLAT.

4. For topside TEC, the largest values in the EIA crests up to ∼158 TECU were registered by the lowest orbiting satellite from the considered set, Spire S155 at ∼320 km altitude, near 22.2 UT (∼14.3 LT) on 10 May 2024. Other satellites registered the EIA enhancements in the crests mostly within the range between 70 and 100 TECU, which was quite significant given that the quiet-time level was primarily ∼30 TECU in topside TEC. In the American sector with available ground-based coverage, the registered topside TEC enhancements contibuted ∼60%–90% into the ground-based TEC.
5. It was found that the EIA crest-to-crest separation expanded to 40°–60° in latitude. In topside TEC, the largest crests separation of 52° and 57° was observed by the lowest Spire S155 satellite at ∼22.1 UT (∼14 LT) near 120°W longitude in the Pacific Ocean and by the Swarm A satellite at ∼22.7 UT (∼19 LT) near 53°W over South America/Brazil. The first satellite overflied the daytime EIA at its most developed state, while the second one encountered the evening sector near sunset, where eastward PPEFs can greatly enhance effects of the PRE of zonal electric fields. The largest crest separation of 60° was observed concurrently in in situ data along this Swarm A satellite overpass at ∼22.7 UT.
6. Jason-3 satellite, measuring the entire ionospheric content between 0 and 1,330 km, registered the largest TEC enhhancements in the EIA crests up to 150–180 TECU (comparing to ∼90 TECU maximum level in quiet time) during 21–24 UT in the American sector and the EIA crests separation was up to 40°–47° in latitude for conditions of ∼16 LT.
7. DMSP satellites revealed significant enhancements of plasma density at ∼850 km altitude between 40°S and 40°N in the American–Pacific sector during the main phase of the storm. They observed clear signatures of the two-peak EIA at those high altitudes with the distance between crests was 31°–41° in latitude and the crest-to-trough ratio varied from 2 to 4. The observed plasma density enhancements in the EIA crests indicate a rise of approximately 4–8 times compared to the quiet-time levels.
8. After ∼21 UT on 10 May 2024, a dramatic large-scale plasma density hole was formed over the magnetic equator in South America (60°–30°W longitude) near local sunset. The in situ plasma density observations from Swarm A and several COSMIC-2 satellites demonstrated a rapid drop of plasma density by several orders of magnitude from ∼3.0 to 3.5×10^6 ion/cm^3 to extremly low levels (under 10^4 ion/cm^3, approaching the lower limit of the instrument sensitivity range), suggesting strong plasma bite-out effects, when the ionospheric F layer was uplifted above the equator to altitudes much higher than satellite orbits. Low-inclination-orbit COSMIC-2 and Spire satellites, traversing through this structure, registered a sharp drop in topside TEC from ∼70 to 95 TECU level down to ∼8–15 TECU.
9. Apart from the significantly intensified EIA expanded in latitude and altitude, the pronounced ionospheric enhancement, associated with SED formation, was observed at low to midlatitudes (0°–40°N) of North America during 21–24 UT on 10 May 2024. In satellite observations, it appeared as a large-scale shoulder-like structure located poleward from the northern crest of the EIA. This structure was detected well in the topside ionosphere, even at DMSP orbit altitudes.
10. The largest ionospheric effects were observed in ground-based TEC and LEO satellite observations during 19–24 UT on 10 May 2024.
11. Finally, Global Electron Content index, calculated from Global Ionospheric Maps of ground-based TEC, revealed a pronounced increase by 20%–30% in the general level of density in the Earth's ionosphere during 19–24 UT on 10 May 2024. It suggests that the storm caused not only the ionospheric plasma redistribution like poleward EIA expansion due to the enhanced equatorial plasma fountain, but actually produced a notable increase of the ionospheric density on a global scale level, considering that this GEC value already includes all concurrent negative storm effects on the night side of the Earth.

Thus, during the storm's main phase (17–03 UT) the ionospheric enhancements (positive storm) started to develop ∼2 hr after the SSC and the most significant ionospheric enhancements were registered between 19 and 24 UT on 10 May 2024. This time window coincided with the prolonged period of the steady southward IMF Bz from ∼19 until 22:31 UT with the minimum value of −43.4 nT at 22:12 UT, along with a steady positive interplanetary electric field dawn-to-dusk component Ey, potentially associated with penetration electric fields from high to equatorial latitudes (Figures 1a and 1d). The long-duration PPEFs are often considered as a primary physical mechanism leading to significant enhancements of ionospheric density and TEC at low and middle latitudes in the early stages of the storms (e.g., Huang, Foster, Goncharenko, et al., 2005; Lin et al., 2005). During intense geomagnetic storms, the dawn-to-dusk electric field will be eastward in direction on the dayside, and thus the PPEFs of eastward polarity can greatly intensify the normal equatorial plasma fountain ($\mathbf{E} \times \mathbf{B}$ plasma drift), leading to so called “super fountain” effect—a phenomenon of dramatic plasma uplift and its subsequent

redistribution from low to mid latitudes under the influence of eastward-directed PPEFs (e.g., Tsurutani et al., 2004, 2008). Due to the significantly larger electric fields, the equatorial plasma on the dayside will be raised to higher altitudes and latitudes than usual. Under such conditions, the EIA can be largely intensified expanding poleward with the crests shifted to midlatitudes (e.g., Abdu, 1997; Balan et al., 2010; Mannucci et al., 2005; Tsurutani et al., 2004). If it occurs in the local time sector with domination of solar ionization production, then plasma densities can be continuously restored at lower altitudes, thus further supporting plasma source for fountain effect and leading to substantial increases observed in density and TEC. As a result of the ionospheric plasma uplift higher into the topside, the plasma gets transported to regions where recombination occurs more slowly, which also assists in keeping TEC levels consistently high. The second outstanding area is the dusk sector, where the eastward PPEFs can have the maximum intensity (e.g., Fejer et al., 2008; Huang, 2023; Richmond et al., 2003) and can overlap the normal PRE fields. Under the combined effect of eastward PPEFs and PRE resulting in a much larger upward $\mathbf{E} \times \mathbf{B}$ drifts, the evening equatorial ionosphere may experience significant uplift causing deep plasma bite-outs of the F region plasma density at the magnetic equator, which can not be restored by production processes due to very late LT. Plasma uplifted to much larger altitudes can further diffuse down along the magnetic field lines with a much larger apex, causing EIA crests to form at locations even more poleward from the magnetic equator than during daytime. Moreover, when the main phase of storms corresponds to dusk conditions in the South Atlantic and the South America/Brazilian sector, these effects may be much stronger due to enhanced conductivity gradient resulting from the energetic particle precipitation in the South Atlantic Magnetic Anomaly region (Abdu et al., 2005, 2008). Thus, eastward PPEFs play the key role in the storm-time EIA intensification and poleward expansion of both EIA crests toward midlatitudes, resulting in large-scale positive ionospheric storm effects during the early stages of geomagnetic storms. However, model simulations demonstrate that storm-time EIA enhancements produced by the PPEF effects on its own can be smaller than those resulting from a combined effect of PPEFs and storm-generated equatorward neutral winds (e.g., Balan et al., 2010; Lin et al., 2005). The equatorward neutral winds can reduce the downward plasma diffusion along magnetic field lines and can rise the ionosphere to higher altitudes with smaller recombination rates—thus, it helps to accumulate plasma and maintain TEC at high level, especially at midlatitudes. Also, the equatorward neutral winds contribute significantly to the formation of SED structure at midlatitudes (e.g., Pokhotelov et al., 2021).

Therefore, the major ionospheric effects registered during the main phase of the May 2024 geomagnetic storm are consistent with the known physical mechanisms and development patterns, which are rather classical for geomagnetic storms in the past (e.g., Wang et al., 2010). The largest positive ionospheric effects occurred at low and middle latitudes in the daytime (14–17 LT) and evening sectors, associated with significant intensification of the EIA under the action of eastward PPEFs. The extreme EIA expansion with crest separation up to 60° in latitude along with the huge plasma bite-out (negative ionospheric response) near the magnetic equator were observed in the dusk/evening sector (19–20 LT) directly over the South America/Brazilian region, where such effects are anticipated to be larger. The huge plasma hole near the equator and the striking shift of the southern EIA crest to very high latitudes over South America were well captured by the GOLD (Global-Scale Observations of the Limb and Disk) UV observations (Karan et al., 2024). According to the ionosonde observations from the equatorial stations in Brazil, the ionospheric F layer rose rapidly to altitudes exceeding 1,000 km in the post-sunset period under the action of eastward-directed PPEFs (e.g., Fagundes, 2024; Resende et al., 2024). Satellites traversing this plasma hole at ∼500 km altitude registered drops to extremely low values of plasma densities. Concurrently, topside TEC observations also revealed a substantial drop (factor of 8–10) in values from ∼70 to 95 TECU level down to ∼8–15 TECU; this level is small, yet non-zero, since topside TEC incorporates both topside ionospheric and plasmaspheric electron contents up to 20,000 km altitude.

The observed ionospheric enhancements up to ∼200 TECU in ground-based TEC and ∼100–155 TECU in the topside TEC were found to be quite high in comparison with the pre-storm quiet time levels. From low to midlatitudes, the daytime ionosphere was found to expand extensively into the topside, thus topside TEC above 400–500 km was the primary contributor into the ground-based TEC (0–20000 km). For example, after 21–22 UT on 10 May 2024, the ground-based TEC showed an increase to ∼190–200 TECU near the northern EIA crest over North America, while the Spire S155 satellite observed here ∼158 TECU, indicating that the topside ionospheric content above ∼320 km altitude constituted about 80% of the ground-based TEC at that time and region. Here in North America, the super fountain effects led to the strongly intensified EIA with the crests already shifted to ∼25° MLAT and the formation of the significant TEC enhancements at low to mid-latitudes just poleward of the

northern EIA crest, further serving as the SED base for the SED plume formation over North America (investigated in detail by Themens et al., 2024; Aa et al., 2024).

The ionospheric disturbances occurred during the main phase of the May 2024 superstorm were very intense and complicated with some extreme (both high and low) values registered in the American sector. However, we should also mention that the observed TEC enhancements can be considered as relatively moderate in comparison with the ionospheric effects of the October 2003 superstorm (SYM-H min of −412 nT). The storm-time ionospheric enhancements did not reach the level of ∼200–300 TECU observed in the topside TEC by CHAMP satellite at ∼400 km orbit altitude while crossing the enhanced EIA crests (at ∼30° MLAT) over the Pacific region at ∼13 LT during the October 2003 superstorm (Mannucci et al., 2005; Tsurutani et al., 2008), as well as the level of ground-based TEC, which exceeded 250 TECU in the SED plume over North America (e.g., Foster & Rideout, 2005). For the case of May 2024 storm, the strongest ionospheric enhancement were observed during 19–24 UT on 10 May 2024, coinciding with a period of the steady southward IMF Bz (near −30 to −40 nT) between 19:05 UT and 22:31 UT and the interplanetary electric field dawn-to-dusk component (IEF Ey), associated with PPEFs, was steady positive (20–26 mV/m). For the 30 October 2003, the spectacular EIA enhancement associated with the super fountain effects due to PPEFs was also registered during a prolonged period of the southward IMF Bz of a quite similar magnitude (near −30 to −35 nT), while the IEF Ey surpassed 40 mV/m (Mannucci et al., 2005; Figure 2). So, the intensity of the eastward electric field, and its effect on the overall TEC increases and ionospheric uplift, was substantially greater during geomagnetic disturbances on 30 October 2003 than on 10 May 2024. Also, the F10.7 flux, which is also correlated with ionospheric ionization levels, reached 237 during the May 2024 storm and much larger value of 275 during the October 2003 storm, whereas the monthly averaged F10.7 values showed the opposite trend (190 in May 2024 vs. 140 in October 2003). Thus, other factors such as preconditioning, seasonal effects, background density level, storm duration (e.g., arrival of multiple consecutive CMEs over several days vs. single event), neutral winds and composition changes, can strongly impact an occurrence and magnitude of the storm-time ionospheric TEC/density enhancements; however, the qualitative and quantitative impacts of those factors cannot be isolated and determined based solely on observational data.

Model simulations are required to identify importance of key physical drivers in generation major ionospheric enhancements of the storm-time EIA, producing differences in altitudinal plasma density redistribution and pronounced asymmetries observed at low and midlatitudes of the Northern and Southern Hemispheres, and this detailed overview of storm-time ionospheric observations from major satellite missions can aid in further model-data comparisons.

Data Availability Statement

The geophysical parameters data are available through the NASA GSFC Space Physics Data Facility's OMNIWeb service (https://omniweb.gsfc.nasa.gov/ow.html), GFZ-Potsdam (https://kp.gfz-potsdam.de/en/; Matzka et al., 2021) and SuperMAG (https://supermag.jhuapl.edu/; Gjerloev, 2012). The IGS Global Ionospheric Maps are available through NASA EarthData portal (https://cddis.nasa.gov/archive/gnss/products/ionex/; login required). Swarm observations are available through the ESA Earth Observation Portal (https://swarm-diss.eo.esa.int/; login required). GRACE-FO data are provided through the Information System and Data Center (ISDC) GFZ-Potsdam (http://isdcftp.gfz-potsdam.de/). COSMIC-2 observations are provided by UCAR COSMIC Data Analysis and Archive Center (CDAAC) (UCAR COSMIC Program, 2019). Spire observations are provided by UCAR CDAAC (https://data.cosmic.ucar.edu/gnss-ro/). DMSP observations are provided through the NOAA National Centers for Environmental Information (NCEI) portal (https://www.ncei.noaa.gov/data/dmsp-space-weather-sensors/access/). Jason-3 observations are available through the NASA Physical Oceanography Distributed Active Archive Center (PO.DAAC) portal at Desai (2016). The GNSS observations are provided by SONEL (https://www.sonel.org), CORS (https://geodesy.noaa.gov/corsdata/rinex), EUREF (https://gnss.bev.gv.at/at.gv.bev.dc/data/obs/), Natural Resources Canada (webapp.geod.nrcan.gc.ca; login required), Canadian High Arctic Ionospheric Network CHAIN (https://chain-new.chain-project.net/data/), SOPAC (http://garner.ucsd.edu/pub/rinex/), Brazilian Network for Continuous Monitoring of the GNSS Systems RBMC (https://geoftp.ibge.gov.br/informacoes_sobre_posicionamento_geodesico/rbmc/), SWEPOS (swepos.lantmateriet.se; login required), IGN France (https://rgp.ign.fr/DONNEES/diffusion/), Instituto Geografico Nacional Espana (https://datos-geodesia.ign.es), Italian Geodetic Data Archiving Facility (geodaf.mt.asi.it), TrigNET (trignet.co.za; login required), RAMSAC

CORS NGI Argentina (https://www.ign.gob.ar/NuestrasActividades/Geodesia/Ramsac/DescargaRinex; Piñón et al., 2018), Australian GNSS Data Center (https://data.gnss.ga.gov.au/docs/home/gnss-data.html).

Acknowledgments
This research was supported by the National Science Foundation (Grant 2054356), National Aeronautics and Space Administration (Grant C22K0658), Air Force Contract FA8803-19-C-0004, and National Oceanic and Atmospheric Administration (Contract NEEA0176, Cooperative Agreement R4310383).

References

Aa, E., Zhang, S. R., Lei, J., Huang, F., Erickson, P. J., Coster, A. J., et al. (2024). Significant midlatitude plasma density peaks and dual-hemisphere SED during the 10–11 May 2024 super geomagnetic storm. *Journal of Geophysical Research: Space Physics*, *129*(11), e2024JA033360. https://doi.org/10.1029/2024JA033360

Abdu, M. A. (1997). Major phenomena of the equatorial ionosphere-thermosphere system under disturbed conditions. *Journal of Atmospheric and Solar-Terrestrial Physics*, *59*(13), 1505–1519. https://doi.org/10.1016/S1364-6826(96)00152-6

Abdu, M. A., Batista, I. S., Carrasco, A. J., & Brum, C. G. M. (2005). South Atlantic magnetic anomaly, ionization: A review and a new focus on electrodynamic effects in the equatorial ionosphere. *Journal of Atmospheric and Solar-Terrestrial Physics*, *67*(17–18), 1643–1657. https://doi.org/10.1016/j.jastp.2005.01.014

Abdu, M. A., De Paula, E. R., Batista, I. S., Reinisch, B. W., Matsuoka, M. T., Camargo, P. O., et al. (2008). Abnormal evening vertical plasma drift and effects on ESF and EIA over Brazil-South Atlantic sector during the 30 October 2003 superstorm. *Journal of Geophysical Research*, *113*(7), A07313. https://doi.org/10.1029/2007JA012844

Abdu, M. A., Maruyama, T., Batista, I. S., Saito, S., & Nakamura, M. (2007). Ionospheric responses to the October 2003 superstorm: Longitude/local time effects over equatorial low and middle latitudes. *Journal of Geophysical Research*, *112*(10), A10306. https://doi.org/10.1029/2006JA012228

Afraimovich, E. L., Astafyeva, E. I., Oinats, A. V., Yasukevich, Y. V., & Zhivetiev, I. V. (2008). Global electron content: A new conception to track solar activity. *Annales Geophysicae*, *26*(2), 335–344. https://doi.org/10.5194/angeo-26-335-2008

Angling, M. J., Nogués-Correig, O., Nguyen, V., Vetra-Carvalho, S., Bocquet, F. X., Nordstrom, K., et al. (2021). Sensing the ionosphere with the Spire radio occultation constellation. *Journal of Space Weather and Space Climate*, *11*(56), 56. https://doi.org/10.1051/swsc/2021040

Astafyeva, E., Zakharenkova, I., & Förster, M. (2015). Ionospheric response to the 2015 St. Patrick's Day storm: A global multi-instrumental overview. *Journal of Geophysical Research: Space Physics*, *120*(10), 9023–9037. https://doi.org/10.1002/2015JA021629

Balan, N., Shiokawa, K., Otsuka, Y., Kikuchi, T., Lekshmi, D. V., Kawamura, S., et al. (2010). A physical mechanism of positive ionospheric storms at low latitudes and midlatitudes. *Journal of Geophysical Research*, *115*(2), A023. https://doi.org/10.1029/2009JA014515

Basu, S., Basu, S., Makela, J. J., Sheehan, R. E., MacKenzie, E., Doherty, P., et al. (2005). Two components of ionospheric plasma structuring at midlatitudes observed during the large magnetic storm of October 30, 2003. *Geophysical Research Letters*, *32*(12), L12S06. https://doi.org/10.1029/2004GL021669

Basu, S. S., Basu, S. S., Groves, K. M., Yeh, H. C., Su, S. Y., Rich, F. J., et al. (2001). Response of the equatorial ionosphere in the South Atlantic region to the great magnetic storm of July 15, 2000. *Geophysical Research Letters*, *28*(18), 3577–3580. https://doi.org/10.1029/2001GL013259

Borries, C., Mahrous, A. M., Ellahouny, N. M., & Badeke, R. (2016). Multiple ionospheric perturbations during the Saint Patrick's Day storm 2015 in the European-African sector. *Journal of Geophysical Research: Space Physics*, *121*(11), 11333–11345. https://doi.org/10.1002/2016JA023178

Buonsanto, M. J. (1999). Ionospheric storms—A review. *Space Science Reviews*, *88*(3/4), 563–601. https://doi.org/10.1023/a:1005107532631

Burns, A. G., Killeen, T. L., Deng, W., Carignan, G. R., & Roble, R. G. (1995). Geomagnetic storm effects in the low- to middle-latitude upper thermosphere. *Journal of Geophysical Research*, *100*(A8), 14673–14691. https://doi.org/10.1029/94ja03232

Carter, B. A., Yizengaw, E., Pradipta, R., Retterer, J. M., Groves, K., Valladares, C., et al. (2016). Global equatorial plasma bubble occurrence during the 2015 St. Patrick's Day storm. *Journal of Geophysical Research: Space Physics*, *121*(1), 894–905. https://doi.org/10.1002/2015JA022194

Cherniak, I., Zakharenkova, I., & Redmon, R. J. (2015). Dynamics of the high-latitude ionospheric irregularities during the 17 March 2015 St. Patrick's Day storm: Ground-based GPS measurements. *Space Weather*, *13*(9), 585–597. https://doi.org/10.1002/2015SW001237

Cherniak, I. V., Zakharenkova, I. E., Dzubanov, D., & Krankowski, A. (2014). Analysis of the ionosphere/plasmasphere electron content variability during strong geomagnetic storm. *Advances in Space Research*, *54*(4), 586–594. https://doi.org/10.1016/j.asr.2014.04.011

Chou, M. Y., Braun, J. J., Wu, Q., Heelis, R. A., Zakharenkova, I., Cherniak, I., et al. (2021). Validation of FORMOSAT-7/COSMIC2 IVM ion density and TGRS orbit electron density. *Terrestrial, Atmospheric and Oceanic Sciences*, *32*(6), 939–951. https://doi.org/10.3319/TAO.2021.06.22.01

Desai, S. (2016). JASON_3_L2_OST_OGDR_GPS [Dataset]. *Ver. F. PO.DAAC*. https://doi.org/10.5067/J3L2G-OGDRF

Doherty, P., Coster, A. J., & Murtagh, W. (2004). Space weather effects of October–November 2003. *GPS Solutions*, *8*(4), 267–271. https://doi.org/10.1007/s10291-004-0109-3

Erickson, P. J., Goncharenko, L. P., Nicolls, M. J., Ruohoniemi, M., & Kelley, M. C. (2010). Dynamics of North American sector ionospheric and thermospheric response during the November 2004 superstorm. *Journal of Atmospheric and Solar-Terrestrial Physics*, *72*(4), 292–301. https://doi.org/10.1016/j.jastp.2009.04.001

Fagundes, P. R. (2024). Study of the ionosphere disturbances due to Coronal Mass Ejection (CME) on May 2024, the strongest geomagnetic storm in the last 2 decades. In *Paper presented at 2024 American Geophysical Union Annual Meeting*. Retrieved from https://agu.confex.com/agu/agu24/meetingapp.cgi/Paper/1511821

Fagundes, P. R., Cardoso, F. A., Fejer, B. G., Venkatesh, K., Ribeiro, B. A. G., & Pillat, V. G. (2016). Positive and negative GPS-TEC ionospheric storm effects during the extreme space weather event of March 2015 over the Brazilian sector. *Journal of Geophysical Research: Space Physics*, *121*(6), 5613–5625. https://doi.org/10.1002/2015JA022214

Fejer, B. G., Jensen, J. W., Kikuchi, T., Abdu, M. A., & Chau, J. L. (2007). Equatorial ionospheric electric fields during the November 2004 magnetic storm. *Journal of Geophysical Research*, *112*(10), A10304. https://doi.org/10.1029/2007JA012376

Fejer, B. G., Jensen, J. W., & Su, S. Y. (2008). Seasonal and longitudinal dependence of equatorial disturbance vertical plasma drifts. *Geophysical Research Letters*, *35*(20), L20106. https://doi.org/10.1029/2008GL035584

Forbes, J. M. (1989). Evidence for the equatorward penetration of electric fields, winds, and compositional effects in the Asian/Pacific sector during the September 17–24, 1984, ETS interval. *Journal of Geophysical Research*, *94*(A12), 16999–17007. https://doi.org/10.1029/ja094ia12p16999

Förster, M., & Jakowski, N. (2000). Geomagnetic storm effects on the topside ionosphere and plasmasphere: A compact tutorial and new results. *Surveys in Geophysics*, *21*(1), 47–87. https://doi.org/10.1023/A:1006775125220

Foster, J. C., & Rideout, W. (2005). Midlatitude TEC enhancements during the October 2003 superstorm. *Geophysical Research Letters*, *32*(12), L12S04. https://doi.org/10.1029/2004GL021719

Fuller-Rowell, T. J., Codrescu, M. V., Moffett, R. J., & Quegan, S. (1994). Response of the thermosphere and ionosphere to geomagnetic storms. *Journal of Geophysical Research*, *99*(A3), 3893–3914. https://doi.org/10.1029/93ja02015

Fuller-Rowell, T. J., Codrescu, M. V., Rishbeth, H., Moffett, R. J., & Quegan, S. (1996). On the seasonal response of the thermosphere and ionosphere to geomagnetic storms. *Journal of Geophysical Research*, *101*(A2), 2343–2353. https://doi.org/10.1029/95JA01614

Gjerloev, J. W. (2012). The SuperMAG data processing technique. *Journal of Geophysical Research*, *117*(A9), A09213. https://doi.org/10.1029/2012JA017683

Gonzalez-Esparza, J. A., Sanchez-Garcia, E., Sergeeva, M., Corona-Romero, P., Gonzalez-Mendez, L. X., Valdes-Galicia, J. F., et al. (2024). The Mother's Day geomagnetic storm on 10 may 2024: Aurora observations and low latitude space weather effects in Mexico. *Space Weather*, *22*(11), e2024SW004111. https://doi.org/10.1029/2024SW004111

Greenspan, M. E., Anderson, P. B., & Pelagatti, J. M. (1986). Characteristics of the thermal plasma monitor (SSIES) for the Defense Meteorological Satellite Program (DMSP) spacecraft F8 through F10, Rep. AFGL-TR-86-0227, DTIC accession number AD A176924, Hanscom Air Force base.

Greenspan, M. E., Rasmussen, C. E., Burke, W. J., & Abdu, M. A. (1991). Equatorial density depletions observed at 840 km during the great magnetic storm of March 1989. *Journal of Geophysical Research*, *96*(A8), 13931–13942. https://doi.org/10.1029/91JA01264

Gulyaeva, T. L., & Veselovsky, I. S. (2012). Two-phase storm profile of global electron content in the ionosphere and plasmasphere of the Earth. *Journal of Geophysical Research*, *117*(9), A0932. https://doi.org/10.1029/2012JA018017

Guo, J. P., Deng, Y., Zhang, D. H., Lu, Y., Sheng, C., & Zhang, S. R. (2018). The effect of subauroral polarization streams on ionosphere and thermosphere during the 2015 St. Patrick's Day storm: Global ionosphere-thermosphere model simulations. *Journal of Geophysical Research: Space Physics*, *123*(3), 2241–2256. https://doi.org/10.1002/2017JA024781

Hairston, M. R., Coley, W. R., & Stoneback, R. (2016). Responses in the polar and equatorial ionosphere to the March 2015 St. Patrick Day storm. *Journal of Geophysical Research: Space Physics*, *121*(11). https://doi.org/10.1002/2016JA023165

Hairston, M. R., & Heelis, R. A. (1996). *Analysis of ionospheric parameters based on DMSP SSIES data using the DBASE4 and NADIA program, Tech. Rep., PL-TR-96-2078*. Phillips Lab., Geophys. Dir., Hanscom Air Force Base, Mass.

Hayakawa, H., Ebihara, Y., Mishev, A., Koldobskiy, S., Kusano, K., Bechet, S., et al. (2025). The solar and geomagnetic storms in May 2024: A flash data report. *The Astrophysical Journal*, *979*(1), 49. https://doi.org/10.3847/1538-4357/ad9335

Heelis, R. A., Stoneback, R. A., Perdue, M. D., Depew, M. D., Morgan, W. A., Mankey, M. W., et al. (2017). Ion velocity measurements for the ionospheric connections explorer. *Space Science Reviews*, *212*(1–2), 615–629. https://doi.org/10.1007/s11214-017-0383-3

Hernández-Pajares, M., Juan, J. M., Sanz, J., Orus, R., Garcia-Rigo, A., Feltens, J., et al. (2009). The IGS VTEC maps: A reliable source of ionospheric information since 1998. *Journal of Geodesy*, *83*(3–4), 263–275. https://doi.org/10.1007/s00190-008-0266-1

Huang, C.-S. (2023). Identification of penetration and disturbance dynamo electric fields and their effects on the generation of equatorial plasma bubbles. *Journal of Geophysical Research: Space Physics*, *128*(11), e2023JA031766. https://doi.org/10.1029/2023JA031766

Huang, C. S., Foster, J. C., Goncharenko, L. P., Erickson, P. J., Rideout, W., & Coster, A. J. (2005). A strong positive phase of ionospheric storms observed by the Millstone Hill incoherent scatter radar and global GPS network. *Journal of Geophysical Research*, *110*(A6), A063. https://doi.org/10.1029/2004JA010865

Huang, C. S., Foster, J. C., & Kelley, M. C. (2005). Long-duration penetration of the interplanetary electric field to the low-latitude ionosphere during the main phase of magnetic storms. *Journal of Geophysical Research*, *110*(A11), A11309. https://doi.org/10.1029/2005JA011202

Huba, J. D., Sazykin, S., & Coster, A. (2017). SAMI3-RCM simulation of the 17 March 2015 geomagnetic storm. *Journal of Geophysical Research: Space Physics*, *122*(1), 1246–1257. https://doi.org/10.1002/2016JA023341

Jakowski, N., Mielich, J., Borries, C., Cander, L., Krankowski, A., Nava, B., & Stankov, S. M. (2008). Large-scale ionospheric gradients over Europe observed in October 2003. *Journal of Atmospheric and Solar-Terrestrial Physics*, *70*(15), 1894–1903. https://doi.org/10.1016/j.jastp.2008.03.020

Jason-3 Products Handbook. (2020). Jason-3 products handbook. Retrieved from https://user.eumetsat.int/s3/eup-strapi-media/pdf_j3_prod_handbook_3cd70eba1b.pdf

Jones, K. L., & Rishbeth, H. (1971). The origin of storm increases of mid-latitude F-layer electron concentration. *Journal of Atmospheric and Terrestrial Physics*, *33*(3), 391–401. https://doi.org/10.1016/0021-9169(71)90144-9

Karan, D. K., Martinis, C. R., Daniell, R. E., Eastes, R. W., Wang, W., McClintock, W. E., et al. (2024). GOLD observations of the merging of the southern crest of the equatorial ionization anomaly and aurora during the 10 and 11 May 2024 Mother's Day super geomagnetic storm. *Geophysical Research Letters*, *51*(15), e2024GL110632. https://doi.org/10.1029/2024GL110632

Kelley, M. C., Vlasov, M. N., Foster, J. C., & Coster, A. J. (2004). A quantitative explanation for the phenomenon known as storm-enhanced density. *Geophysical Research Letters*, *31*(19), 3–5. https://doi.org/10.1029/2004GL020875

Kil, H., Lee, W. K., Paxton, L. J., Hairston, M. R., & Jee, G. (2016). Equatorial broad plasma depletions associated with the evening prereversal enhancement and plasma bubbles during the 17 March 2015 storm. *Journal of Geophysical Research: Space Physics*, *121*(10), 10209–10219. https://doi.org/10.1002/2016JA023335

Klimenko, M. V., Klimenko, V. V., Despirak, I. V., Zakharenkova, I. E., Kozelov, B. V., Cherniakov, S. M., et al. (2018). Disturbances of the thermosphere-ionosphere-plasmasphere system and auroral electrojet at 30°E longitude during the St. Patrick's Day geomagnetic storm on 17–23 March 2015. *Journal of Atmospheric and Solar-Terrestrial Physics*, *180*(December 2017), 78–92. https://doi.org/10.1016/j.jastp.2017.12.017

Klimenko, M. V., Zakharenkova, I. E., Klimenko, V. V., Lukianova, R. Y., & Cherniak, I. V. (2019). Simulation and observations of the polar tongue of ionization at different heights during the 2015 St. Patrick's Day storms. *Space Weather*, *17*(7), 1073–1089. https://doi.org/10.1029/2018SW002143

Krankowski, A., Shagimuratov, I. I., Baran, L. W., & Yakimova, G. (2007). The structure of the mid- and high-latitude ionosphere during the November 2004 storm event obtained from GPS observations. *Acta Geophysica*, *55*(4), 490–508. https://doi.org/10.2478/s11600-007-0033-3

Lei, J., Thayer, J. P., Burns, A. G., Lu, G., & Deng, Y. (2010). Wind and temperature effects on thermosphere mass density response to the November 2004 geomagnetic storm. *Journal of Geophysical Research*, *115*(5), 1–18. https://doi.org/10.1029/2009JA014754

Lei, J., Wang, W., Burns, A. G., Solomon, S. C., Richmond, A. D., Wiltberger, M., et al. (2008). Observations and simulations of the ionospheric and thermospheric response to the December 2006 geomagnetic storm: Initial phase. *Journal of Geophysical Research*, *113*(A1), A01314. https://doi.org/10.1029/2007JA012807

Lei, J., Wang, W., Burns, A. G., Yue, X., Dou, X., Luan, X., et al. (2014). New aspects of the ionospheric response to the October 2003 superstorms from multiple-satellite observations. *Journal of Geophysical Research: Space Physics*, *119*(3), 2298–2317. https://doi.org/10.1002/2013JA019575

Lin, C. H., Richmond, A. D., Heelis, R. A., Bailey, G. J., Lu, G., Liu, J. Y., et al. (2005). Theoretical study of the low- and midlatitude ionospheric electron density enhancement during the October 2003 superstorm: Relative importance of the neutral wind and the electric field. *Journal of Geophysical Research*, *110*(A12), A12312. https://doi.org/10.1029/2005JA011304

Liu, H., & Lühr, H. (2005). Strong disturbance of the upper thermospheric density due to magnetic storms: CHAMP observations. *Journal of Geophysical Research*, *110*(A9), A09S29. https://doi.org/10.1029/2004JA010908

Liu, J., Wang, W., Burns, A., Yue, X., Zhang, S., Zhang, Y., & Huang, C. (2016). Profiles of ionospheric storm-enhanced density during the 17 March 2015 great storm. *Journal of Geophysical Research: Space Physics*, *121*(1), 727–744. https://doi.org/10.1002/2015JA021832

Lu, G., Zakharenkova, I., Cherniak, I., & Dang, T. (2020). Large-scale ionospheric disturbances during the 17 March 2015 storm: A model-data comparative study. *Journal of Geophysical Research: Space Physics*, *125*(5), e2019JA027726. https://doi.org/10.1029/2019JA027726

Mannucci, A. J., Tsurutani, B. T., Iijima, B. A., Komjathy, A., Saito, A., Gonzalez, W. D., et al. (2005). Dayside global ionospheric response to the major interplanetary events of October 29–30, 2003 "Halloween Storms.". *Geophysical Research Letters*, *32*(12), L12S02. https://doi.org/10.1029/2004GL021467

Mannucci, A. J., Tsurutani, B. T., Kelley, M. C., Iijima, B. A., & Komjathy, A. (2009). Local time dependence of the prompt ionospheric response for the 7, 9, and 10 November 2004 superstorms. *Journal of Geophysical Research*, *114*(10), 1–13. https://doi.org/10.1029/2009JA014043

Matzka, J., Bronkalla, O., Tornow, K., Elger, K., & Stolle, C. (2021). Geomagnetic Kp index. V. 1.0 [Dataset]. *GFZ Data Services*. https://doi.org/10.5880/Kp.0001

Mendillo, M. (2006). Storms in the ionosphere: Patterns and processes for total electron content. *Reviews of Geophysics*, *44*(4), RG4001. https://doi.org/10.1029/2005RG000193

Mitchell, C. N., Alfonsi, L., De Franceschi, G., Lester, M., Romano, V., & Wernik, A. W. (2005). GPS TEC and scintillation measurements from the polar ionosphere during the October 2003 storm. *Geophysical Research Letters*, *32*(12), 1–4. https://doi.org/10.1029/2004GL021644

Namgaladze, A. A., Förster, M., & Yurik, R. Y. (2000). Analysis of the positive ionospheric response to a moderate geomagnetic storm using a global numerical model. *Annales Geophysicae*, *18*(4), 461–477. https://doi.org/10.1007/s00585-000-0461-8

Newell, P. T., & Gjerloev, J. W. (2011). Evaluation of SuperMAG auroral electrojet indices as indicators of substorms and auroral power. *Journal of Geophysical Research*, *116*(12), 1–12. https://doi.org/10.1029/2011JA016779

Ozturk, D. S., Zou, S., Ridley, A. J., & Slavin, J. A. (2018). Modeling study of the geospace system response to the solar wind dynamic pressure enhancement on 17 March 2015. *Journal of Geophysical Research: Space Physics*, *123*(4), 2974–2989. https://doi.org/10.1002/2017JA025099

Pavlov, A. V., & Foster, J. C. (2001). Model/data comparison of F region ionospheric perturbation over Millstone Hill during the severe geomagnetic storm of July 15–16, 2000. *Journal of Geophysical Research*, *106*(A12), 29051–29069. https://doi.org/10.1029/2000ja000387

Pedatella, N. M., Zakharenkova, I., Braun, J. J., Cherniak, I., Hunt, D., Schreiner, W. S., et al. (2021). Processing and validation of FORMOSAT-7/COSMIC-2 GPS total electron content observations. *Radio Science*, *56*(8), 1–15. https://doi.org/10.1029/2021RS007267

Pedatella, N. M., Zakharenkova, I., Braun, J. J., Cherniak, I., Hunt, D., Schreiner, W. S., et al. (2023). Processing and validation of FORMOSAT-7/COSMIC-2 GLONASS total electron content observations. *Radio Science*, *58*(6), e2022RS007589. https://doi.org/10.1029/2022RS007589

Piñón, D. A., Gómez, D. D., Smalley, R., Cimbaro, S. R., Lauría, E. A., & Bevis, M. G. (2018). The history, state, and future of the argentine continuous satellite monitoring network and its contributions to geodesy in Latin America. *Seismological Research Letters*, *89*(2A), 475–482. https://doi.org/10.1785/0220170162

Pokhotelov, D., Fernandez-Gomez, I., & Borries, C. (2021). Polar tongue of ionisation during geomagnetic superstorm. *Annales Geophysicae*, *39*(5), 833–847. https://doi.org/10.5194/angeo-39-833-2021

Prikryl, P., Ghoddousi-Fard, R., Weygand, J. M., Viljanen, A., Connors, M., Danskin, D. W., et al. (2016). GPS phase scintillation at high latitudes during the geomagnetic storm of 17–18 March 2015. *Journal of Geophysical Research: Space Physics*, *121*(10), 10448–10465. https://doi.org/10.1002/2016JA023171

Prölss, G. W. (1995). Ionospheric F region storms. In H. Volland (Ed.), *Handbook of Atmospheric Electrodynamics* (Vol. 2, pp. 195–248). CRC Press.

Resende, L. C. A., Zhu, Y., Santos, A. M., Chagas, R. A. J., Denardini, C. M., Arras, C., et al. (2024). Nocturnal Sporadic Cusp-Type Layer (Esc) resulting from anomalous excess ionization over the SAMA region during the extreme magnetic storm on 11 May 2024. *Journal of Geophysical Research: Space Physics*, *129*(11), e2024JA033167. https://doi.org/10.1029/2024JA033167

Retterer, J. M., Ilma, R., Kelley, M. C., Chau, J. L., Valladares, C. E., Gentile, L. C., & Groves, K. (2010). Modeling the low-latitude ionospheric electron density and plasma turbulence in the November 2004 storm period. *Journal of Atmospheric and Solar-Terrestrial Physics*, *72*(4), 350–357. https://doi.org/10.1016/j.jastp.2009.07.012

Review of Swarm L1B data quality. (2020). Review of Swarm L1B data quality. Retrieved from https://earth.esa.int/eogateway/documents/20142/37627/Swarm-L1B-data-quality-review.pdf

Richmond, A. D., & Lu, G. (2000). Upper-atmospheric effects of magnetic storms: A brief tutorial. *Journal of Atmospheric and Solar-Terrestrial Physics*, *62*(12), 1115–1127. https://doi.org/10.1016/S1364-6826(00)00094-8

Richmond, A. D., Peymirat, C., & Roble, R. G. (2003). Long-lasting disturbances in the equatorial ionospheric electric field simulated with a coupled magnetosphere-ionosphere-thermosphere model. *Journal of Geophysical Research*, *108*(A3), 1118. https://doi.org/10.1029/2002JA009758

Schreiter, L., Stolle, C., Rauberg, J., Kervalishvili, G., van den Ijssel, J., Arnold, D., et al. (2023). Topside ionosphere sounding from the CHAMP, GRACE, and GRACE-FO missions. *Radio Science*, *58*(3). https://doi.org/10.1029/2022RS007552

Swarm L2 TEC Product Description. (2017). Retrieved from https://earth.esa.int/eogateway/documents/20142/37627/swarm-level-2-tec-product-description.pdf

Themens, D. R., Elvidge, S., McCaffrey, A. M., Jayachandran, P. T., Coster, A., Varney, R. H., et al. (2024). The high latitude ionospheric response to the major May 2024 geomagnetic storm: A synoptic view. *Geophysical Research Letters*, *51*(19), e2024GL111677. https://doi.org/10.1029/2024GL111677

Tsurutani, B., Mannucci, A., Iijima, B., Abdu, M. A., Sobral, J. H. A., Gonzalez, W., et al. (2004). Global dayside ionospheric uplift and enhancement associated with interplanetary electric fields. *Journal of Geophysical Research*, *109*(A8), A08302. https://doi.org/10.1029/2003JA010342

Tsurutani, B. T., Judge, D. L., Guarnieri, F. L., Gangopadhyay, P., Jones, A. R., Nuttall, J., et al. (2005). The October 28, 2003 extreme EUV solar flare and resultant extreme ionospheric effects: Comparison to other Halloween events and the Bastille Day event. *Geophysical Research Letters*, *32*(3), L03S09. https://doi.org/10.1029/2004GL021475

Tsurutani, B. T., Verkhoglyadova, O. P., Mannucci, A. J., Lakhina, G. S., & Huba, J. D. (2012). Extreme changes in the dayside ionosphere during a Carrington-type magnetic storm. *Journal of Space Weather and Space Climate*, *2*, A05. https://doi.org/10.1051/swsc/2012004

Tsurutani, B. T., Verkhoglyadova, O. P., Mannucci, A. J., Saito, A., Araki, T., Yumoto, K., et al. (2008). Prompt penetration electric fields (PPEFs) and their ionospheric effects during the great magnetic storm of 30-31 October 2003. *Journal of Geophysical Research*, *113*(5). https://doi.org/10.1029/2007JA012879

UCAR COSMIC Program. (2019). COSMIC-2 data products [Dataset]. *UCAR/NCAR – COSMIC*. https://doi.org/10.5065/T353-C093

Verkhoglyadova, O. P., Meng, X., Mannucci, A. J., Mlynczak, M. G., Hunt, L. A., & Lu, G. (2017). Ionosphere-thermosphere energy budgets for the ICME storms of March 2013 and 2015 estimated with GITM and observational proxies. *Space Weather*, *15*(9), 1102–1124. https://doi.org/10.1002/2017SW001650

Wang, W., Lei, J., Burns, A. G., Solomon, S. C., Wiltberger, M., Xu, J., et al. (2010). Ionospheric response to the initial phase of geomagnetic storms: Common features. *Journal of Geophysical Research*, *115*(7), A07321. https://doi.org/10.1029/2009JA014461

Weiss, J. P., Schreiner, W. S., Braun, J. J., Xia-Serafino, W., & Huang, C. Y. (2022). COSMIC-2 mission summary at three years in orbit. *Atmosphere*, *13*(9), 1409. https://doi.org/10.3390/atmos13091409

Wu, Q., Pedatella, N. M., Braun, J. J., Schreiner, W., Weiss, J., Chou, M.-Y., et al. (2022). Comparisons of ion density from IVM with the GNSS differential TEC-derived electron density on the FORMOSAT-7/COSMIC-2 mission. *Journal of Geophysical Research: Space Physics*, *127*(8), e2022JA030392. https://doi.org/10.1029/2022JA030392

Xiong, C., Park, J., Lühr, H., Stolle, C., & Ma, S. Y. (2010). Comparing plasma bubble occurrence rates at CHAMP and GRACE altitudes during high and low solar activity. *Annales Geophysicae*, *28*(9), 1647–1658. https://doi.org/10.5194/angeo-28-1647-2010

Yizengaw, E., Moldwin, M. B., Dyson, P. L., & Immel, T. J. (2005). Southern Hemisphere ionosphere and plasmasphere response to the interplanetary shock event of 29–31 October 2003. *Journal of Geophysical Research*, *110*(A9), A09S30. https://doi.org/10.1029/2004JA010920

Zakharenkova, I., Astafyeva, E., & Cherniak, I. (2016). GPS and GLONASS observations of large-scale traveling ionospheric disturbances during the 2015 St. Patrick's Day storm. *Journal of Geophysical Research: Space Physics*, *121*(12), 12138–12156. https://doi.org/10.1002/2016JA023332

Zhang, S. R., Erickson, P. J., Zhang, Y., Wang, W., Huang, C., Coster, A. J., et al. (2017). Observations of ion-neutral coupling associated with strong electrodynamic disturbances during the 2015 St. Patrick's Day storm. *Journal of Geophysical Research: Space Physics*, *122*(1), 1314–1337. https://doi.org/10.1002/2016JA023307